AGU PUBLICATIONS

JGR

Journal of Geophysical Research: Solid Earth

RESEARCH ARTICLE
10.1002/2015JB012230

Key Points:
- Characterization of short and long-wavelength deformation as small as 2 mm/yr with InSAR
- Refined estimates of along-fault surface creep rates for the Hayward and Calaveras Faults
- Estimates of long-term and shallow slip rates and earthquake potential on Hayward and Calaveras

Supporting Information:
- Table S1 and Figures S1–S8

Correspondence to:
E. Chaussard,
estelle@seismo.berkeley.edu

Citation:
Chaussard, E., R. Bürgmann, H. Fattahi, C. W. Johnson, R. Nadeau, T. Taira, and I. Johanson (2015), Interseismic coupling and refined earthquake potential on the Hayward-Calaveras fault zone, *J. Geophys. Res. Solid Earth*, *120*, doi:10.1002/2015JB012230.

Received 21 MAY 2015
Accepted 31 OCT 2015
Accepted article online 11 NOV 2015

Interseismic coupling and refined earthquake potential on the Hayward-Calaveras fault zone

E. Chaussard[1,2,3], R. Bürgmann[1,2], H. Fattahi[4], C. W. Johnson[1,2], R. Nadeau[1,2], T. Taira[1,2], and I. Johanson[1,2]

[1]Department of Earth and Planetary Science, University of California, Berkeley, California, USA, [2]Berkeley Seismological Laboratory, University of California, Berkeley, California, USA, [3]Now at Department of Geology, State University of New York, Buffalo, New York, USA, [4]Seismological Laboratory, California Institute of Technology, Pasadena, California, USA

Abstract Interseismic strain accumulation and fault creep is usually estimated from GPS and alignment arrays data, which provide precise but spatially sparse measurements. Here we use interferometric synthetic aperture radar to resolve the interseismic deformation associated with the Hayward and Calaveras Faults (HF and CF) in the East San Francisco Bay Area. The large 1992–2011 SAR data set permits evaluation of short- and long-wavelength deformation larger than 2 mm/yr without alignment of the velocity field to a GPS-based model. Our time series approach in which the interferogram selection is based on the spatial coherence enables deformation mapping in vegetated areas and leads to refined estimates of along-fault surface creep rates. Creep rates vary from 0 ± 2 mm/yr on the northern CF to 14 ± 2 mm/yr on the central CF south of the HF surface junction. We estimate the long-term slip rates by inverting the long-wavelength deformation and the distribution of shallow slip due to creep by inverting the remaining velocity field. This distribution of slip reveals the locations of locked and slowly creeping patches with potential for a $M6.8 \pm 0.3$ on the HF near San Leandro, a $M6.6 \pm 0.2$ on the northern CF near Dublin, a $M6.5 \pm 0.1$ on the HF south of Fremont, and a $M6.2 \pm 0.2$ on the central CF near Morgan Hill. With cascading multisegment ruptures the HF rupturing from Berkeley to the CF junction could produce a $M6.9 \pm 0.1$, the northern CF a $M6.6 \pm 0.1$, the central CF a $M6.9 \pm 0.2$ from the junction to Gilroy, and a joint rupture of the HF and central CF could produce a $M7.1 \pm 0.1$.

1. Introduction

The San Andreas fault system includes several right-lateral strands in the San Francisco Bay Area, the Calaveras and Hayward Faults (CF, and HF, respectively) being the dominant structures in the East Bay and accommodating ~15 mm/yr (~30%) of the relative motion between the North American and Pacific plates [*Field et al*., 2015]. These faults lie near major urban areas including Oakland, Fremont, San Jose, and Livermore and have the potential to cause significant loss of life and property given their historical activity. Since 1850, there have been 13 earthquakes $M \geq 5$ on the CF [*Oppenheimer et al*., 2010] and 4 on the HF [*Toppozada et al*., 2002], illustrating this significant seismic hazard [*Field et al*., 2015]. *Chaussard et al*. [2015] recently showed that the HF and the CF are directly connected on the surface and at depth, suggesting that earthquake ruptures could encompass both faults leading to potential for earthquakes with $M > 7$. However, both the HF and the CF display active surface creep at spatially variable rates, indicating a complex distribution of locked and shallow slipping patches. Accordingly, to precisely refine the earthquake potential of the Hayward-Calaveras fault zone (HCFZ), characterization of the creep rates along the faults with a high spatial resolution is necessary.

The HCFZ considered here encompasses the HF, the northern CF, and the central CF from the junction with the northern CF to Gilroy (Figure 1). The 2 to 8 mm/yr range of creep rates along the HF is well documented by over 30 alignment arrays (AAs) and 5 creepmeters covering the 60 km distance between Point Pinole and Fremont [*Lienkaemper et al*., 2014; *Bilham et al*., 2004]. Additionally, the distribution of locking and shallow slip due to creep in space and time has been studied along the urban sections of the HF relying on inversion of InSAR (interferometric synthetic aperture radar) data [*Schmidt et al*., 2005; *Shirzaei and Bürgmann*, 2013]. Creep on the north and central CF is not as well constrained because the fault traces largely lie in vegetated and hilly terrain, limiting remote sensing capabilities, and only nine AAs exist on this fault over a length of

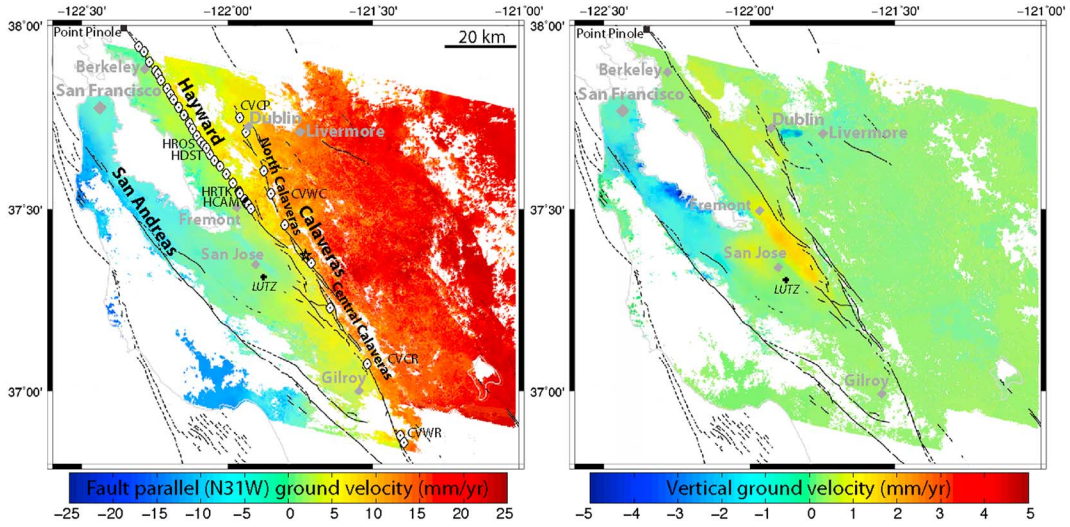

Figure 1. (left) InSAR mean velocity field in the San Francisco Bay Area showing the HF-CF-parallel (N31°W) deformation. The mean velocity map covers the area of track 70 frame 2853 (west) (already presented in *Chaussard et al.* [2015]) and track 299 frame 2853 (east). Blue colors show northwest motion and red colors southeast motion with respect to GPS station LUTZ (cross). Interseismic surface creep across the HF and CF are marked by sharp transitions in colors. Solid and dashed black lines indicate mapped fault traces, white diamonds indicate the locations of AAs, the black star shows the location of the connection between the HF and CF surface traces, the black box at the top indicates the location of Point Pinole, taken as reference for along-fault measurements, and grey diamonds are major cities. The AAs whose time series are shown in Figure 6 are labeled for reference. (right) Mean vertical ground velocity, most of the deformation is local and due to hydrological processes. Blue colors correspond to subsidence and red colors to uplift.

~100 km. The AAs suggest slow and episodic (<2 mm/yr) creep on the northern section of the northern CF, increasing to steady creep at ~4 mm/yr near the transition with the central CF [*Lienkaemper et al.*, 2014]. Small aperture networks suggest creep rates between 3 to 7 mm/yr in the northern section of the central CF [*Prescott and Lisowski*, 1983] and AAs suggest creep rates of ~10 mm/yr to the south [*Lienkaemper et al.*, 2014]. We aim to refine the along-HCFZ creep rate variability by using a large InSAR data set and a modified time series method directly accounting for the spatial coherence [*Chaussard et al.*, 2015], allowing for creep estimations not only in urban areas [*Schmidt et al.*, 2005; *Shirzaei and Bürgmann*, 2013] but also on vegetated hillsides.

Reassessing the earthquake potential on the HCFZ also requires precise characterization of the long-term fault slip rates (loading rates) from the interseismic strain accumulation. Strain accumulation increases the seismic moment potential with time, in opposition to the effect of fault creep, which aseismically releases accumulated strain, thereby reducing the seismic potential. Thus, to refine estimates of seismic hazard it is necessary to evaluate how the aseismic fault slip distribution compares to the long-term slip rates. Evaluation of interseismic strain accumulation (long-wavelength deformation) traditionally relies on GPS, providing precise but spatially sparse measurements [e.g., *d'Alessio et al.*, 2005]. Sometimes such GPS data sets are used to align InSAR velocity fields, which improve the spatial coverage [*Bürgmann et al.*, 2006; *Fialko*, 2006; *Tong et al.*, 2013; *Shirzaei and Bürgmann*, 2013]. However, in this approach the two data sets become intrinsically dependent and the GPS data cannot be used to evaluate the uncertainty of the InSAR velocity field. Additionally, InSAR contributes only short-wavelength information (near-fault deformation), the long-wavelength deformation signal being removed during the image processing. Our time series analysis of a large InSAR data set allows us to characterize short- and long-wavelength horizontal deformation in the San Francisco Bay Area, without any alignment to a GPS velocity field or an a priori model of deformation. The independent GPS and AA data sets are instead used to estimate the level of accuracy of the InSAR velocity field and time series. With this approach, high spatial resolution InSAR velocity fields can be used to characterize interseismic deformation even in areas with limited GPS coverage. Estimates of the faults' long-term slip rates are then obtained by inversion of the InSAR-constrained long-wavelength horizontal surface velocities (assuming to be due to elastic strain accumulation and validated with the independent GPS measurements), while inversion of the remaining near-fault motion after removal of the long-wavelength

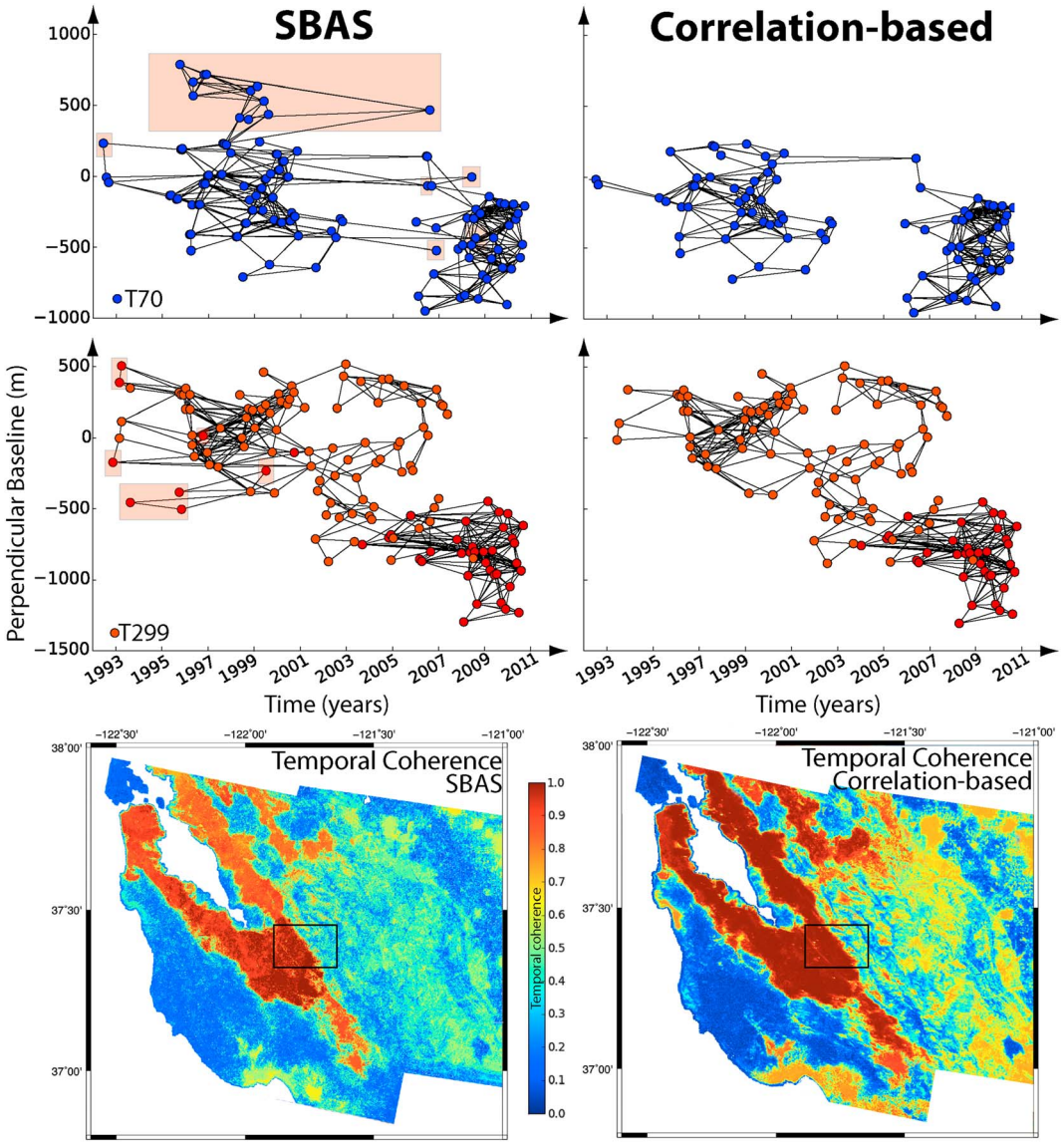

Figure 2. Comparison between SBAS (left) and our correlation-based selection (right) using only interferograms with over 50% of pixels with correlation >0.5 in the selected area of interest (black box on Figure 2, bottom). (top) baseline plots for tracks 70 (blue) and 299 (red) with the red boxes highlighting the SAR acquisitions removed by the correlation-based selection. (bottom) resulting temporal coherence maps.

deformation provides constraints on the shallow aseismic slip rates. We validate the distribution of the InSAR-inverted shallow slip by comparing with the distribution and cumulative slip of characteristically repeating earthquakes (CREs) occurring on the HCFZ [*Bürgmann et al*., 2000; *Peng et al*., 2005; *Templeton et al*., 2009; *Chaussard et al*., 2015]. Using the deficit between the shallow slip rates and the long-term slip rates we evaluate the moment magnitude deficit on the HCFZ sections, information that is necessary for earthquake hazard assessment.

2. Method

2.1. Mean InSAR Velocity map

2.1.1. Long-Wavelength Deformation

To characterize the HCFZ creep and strain accumulation with an InSAR velocity field we must overcome two challenges. First, orbital errors result in long-wavelength noise (ramps) in interferograms, which are larger

than the interseismic signal [e.g., *Bürgmann et al*., 2006; *Fialko*, 2006; *Gourmelen et al*., 2010; *Tong et al*., 2013]. However, when integrating tens or more SAR acquisitions through time series analysis, long-wavelength deformation of a few millimeters per year per hundred kilometers can be detected [*Fattahi and Amelung*, 2014]. Accordingly, with a data set larger than ~50 SAR acquisitions long-wavelength deformation should be resolvable without removing any orbital ramps (except the Envisat advanced synthetic aperture radar (ASAR) Local Oscillator drift (LOD) correction) and without aligning the InSAR velocity field to GPS-based model of deformation.

We used over 250 SAR images acquired by the ERS-1-ERS-2 and Envisat satellites of the European Space Agency to resolve the 1992–2011 interseismic deformation in the San Francisco Bay Area (supporting information Table S1). We relied on data from four tracks (two descending: 70 and 299 and two ascending: 206 and 478) and six frames (2853 on descending tracks and 729 and 747 on ascending tracks) provided through the Western North American interferometric synthetic aperture radar consortium (WInSAR) archive (supporting information Figure S1). By combining these SAR acquisitions in the time series analysis, after the Envisat LOD correction and given the orbital accuracy, the precision of the InSAR measurements is on the order of 1.3 mm/yr/100 km, which enables detection of long-wavelength deformation [*Fattahi and Amelung*, 2014].

The LOD corresponds to a slow decay of the Envisat ASAR's Local Oscillator frequency with respect to its nominal value. It results in a linear and correlated-in-time phase trend equivalent to ~15 mm/yr of deformation (from near to far range). On the opposite, in ERS data the LOD is random from epoch to epoch and thus is effectively random noise. We used the empirical model of *Marinkovic and Larsen* [2013] to correct for the Envisat ASAR LOD, which adjusts the range-change history for each pixel with a correction $C = (3.87 \times 10^{-7})$ $x\delta\rho\delta t$ with x the dimensionless pixel count in range direction, $\delta\rho$ the range pixel size, and δt the time difference between a given epoch and the reference epoch. With the Envisat LOD appropriately corrected, time series of InSAR data are capable of accurately measuring long-wavelength deformation [*Fattahi and Amelung*, 2014]. The remaining noise contains small orbital errors and contributions from atmospheric delay, modest given the large number of data used. We used the processing technique described by *Chaussard et al*. [2015], but instead of focusing on the HF-CF junction, we extended the area to the east to resolve the interseismic deformation associated with the CF (*Chaussard et al*. [2015] showed only the mean velocity map for the area of track 70 frame 2853, we added the area of track 299 to the east).

Single Look Complex data were produced relying on the Modular SAR Processor software and over 3600 interferograms were generated with the ROI_PAC software [*Rosen et al*., 2004]. The 1 arc sec digital elevation model from the Shuttle Radar Topography Mission [*Farr et al*., 2007] was used to remove topographic contributions. For each frame, the interferograms were coregistered to a master image, unwrapped using SNAPHU [*Chen and Zebker*, 2001], and referenced to the same pixel, collocated with the GPS station LUTZ. A least square approach (Small Baseline Subset, SBAS) was applied to a fully connected networks of interferograms to retrieve the phase history at each epoch relative to the first [*Berardino et al*., 2002].

2.1.2. Coherence

The second challenge is preserving coherence across the CF where urban areas are replaced by vegetated hills. We used the alternative selection method described by *Chaussard et al*. [2015] in which only SAR acquisitions leading to interferograms with 50% of pixels with a spatial correlation >0.5 in an area of interest comprising vegetated hillsides across the CF (black rectangle in Figure 2 (bottom)), are used in the time series analysis (~1200 interferograms). With this correlation-based selection the temporal coherence in the mean velocity map east of the CF rises from ~0.3 with standard SBAS selection to >0.5 (Figure 2). The better temporal coherence reflects a narrower selection than the SBAS one with the removal of interferograms and SAR acquisitions that lead to low coherence (due to atmospheric effects and seasonal variations in vegetation).

After the inversion, topographic residuals were corrected in the time domain [*Fattahi and Amelung*, 2013] and the final pixel selection was based on a temporal coherence threshold of 0.5 [*Pepe and Lanari*, 2006]. This threshold is lower than the ones of previous studies [*Casu et al*., 2006; *Tizzani et al*., 2007; *Gourmelen et al*., 2010], but velocities at pixels of coherence 0.5–0.7 and >0.7 were validated with GPS data (section 2.2.2). A much higher spatial coverage is achieved east of the CF with this method compared to previous works (supporting information Figure S2) [*Bürgmann et al*., 2006; *Shirzaei and Bürgmann*, 2013; *Chaussard et al*., 2014]. A disadvantage of the correlation-based selection is that some SAR acquisitions must be discarded, leading to a lower temporal sampling (Figure 2 (top), red boxes).

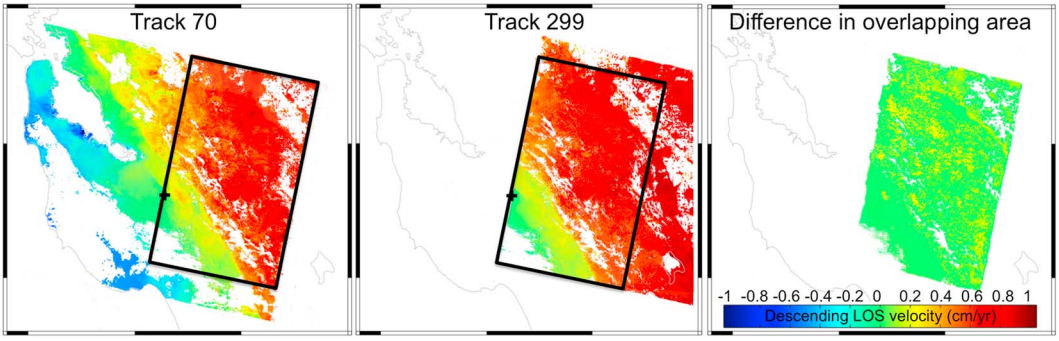

Figure 3. Comparison between mean LOS velocity maps of two neighboring descending tracks (70 and 299) referenced to LUTZ (black cross). The black rectangle highlights the overlapping area. The good agreement between the two independently processed tracks confirms the low noise level of the mean velocity maps.

2.2. Noise Level and Validation of the Velocity Field

2.2.1. Neighboring InSAR Tracks

First, the line-of-sight (LOS) InSAR velocity fields were validated by comparing results from two adjacent descending tracks (70 and 299) that overlap by 4800 km^2. The different viewing geometries of these tracks were accounted for by using a common datum, track 70 being a "master track" and track 299 as a "slave track" [*Ketelaar et al*., 2007]. The difference in incidence angle was accounted for similarly to the digital elevation model error removal [*Shirzaei*, 2015]. In this overlapping area the average absolute difference between the two tracks is 0.3 mm/yr. This observation confirms that the InSAR velocity maps are representative of deformation with a low noise level (Figure 3).

2.2.2. BAVU3 GPS

To compare InSAR velocities with independent data sets (horizontal GPS velocities and AA surface creep rates), we must first obtain measurements of horizontal motion. We followed the approach of *Wright et al*. [2004] and used ascending and descending velocity maps to decompose the signal into its vertical and fault-parallel components, assuming that the fault-perpendicular motion is zero. Figure 1 shows the horizontal velocity field projected into motion parallel to the average strike of the HF and CF (N31°W) and the vertical

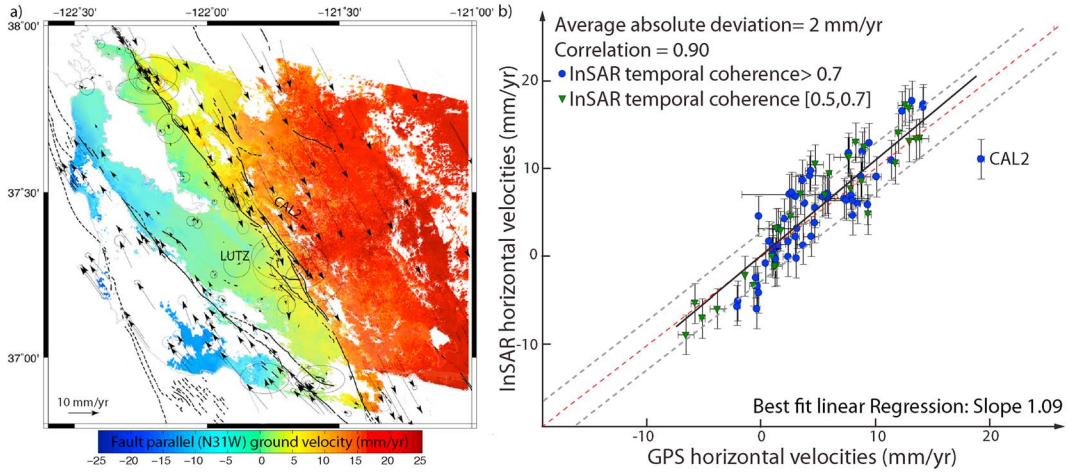

Figure 4. (a) Comparison between InSAR fault-parallel velocities and fault-parallel BAVU3 GPS velocities (black arrows on Figure 4a) relative to centrally located station LUTZ for the same area presented in Figure 1 (tacks 70 and 299; *Chaussard et al*. [2015] presented the comparison only for the area covered by track 70). (b) InSAR velocities are mean rate for pixels within 200 m from each GPS station. The blue circles show pixels with a temporal coherence >0.7 in the InSAR velocity map, the green triangles pixels with a temporal coherence between 0.5 and 0.7. The strong outlier corresponds to the station CAL2 with anomalous GPS velocities. The best fit linear regression is shown by a full black line, the red dashed line shows a 1 to 1 linear regression, and the grey dashed lines show deviation of 2 mm/yr.

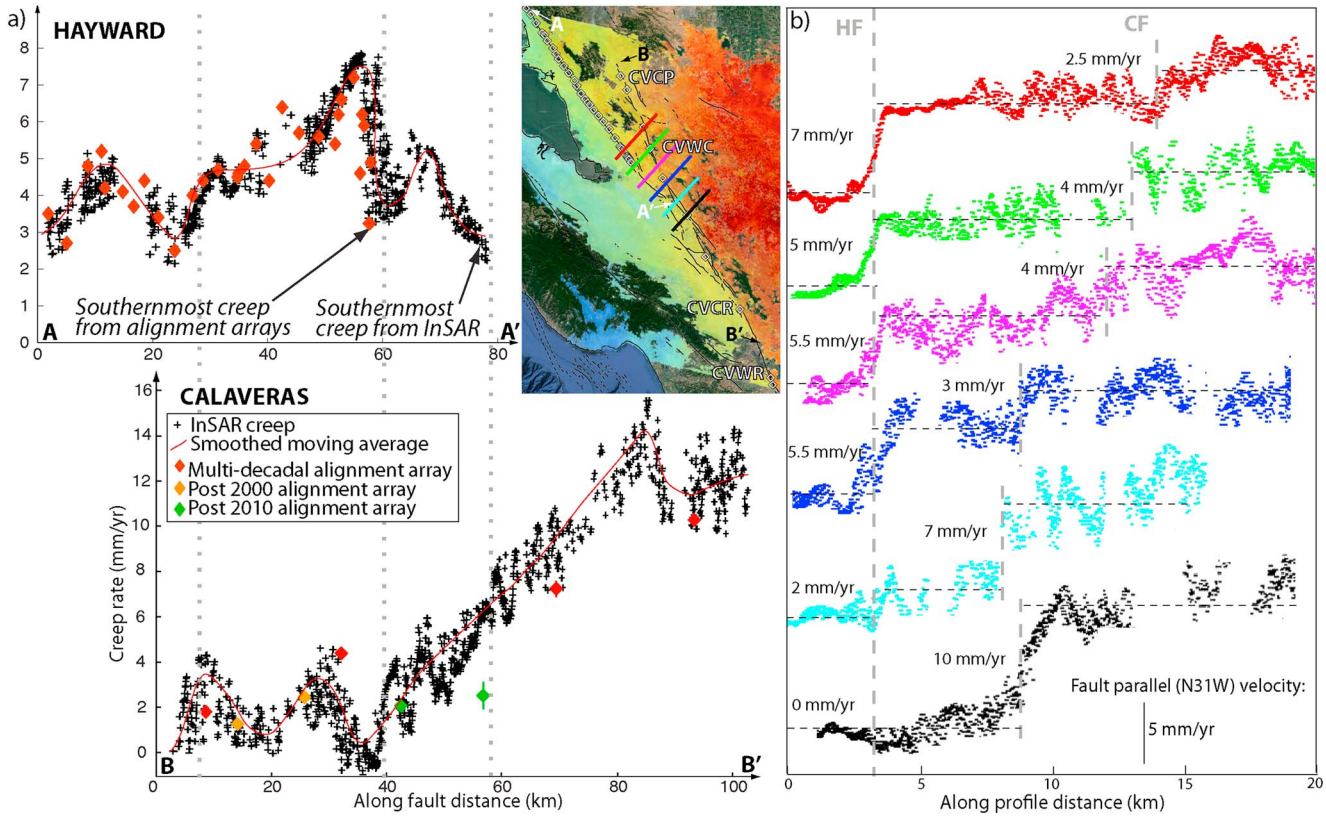

Figure 5. (a) Along-fault creep rates for HF (top) and CF (bottom). The diamonds are the AAs data color coded according to their temporal coverage. The AA uncertainties are shown with vertical bars but are mostly smaller than the marker size, the InSAR scatter (black crosses) illustrates the relative uncertainty. (b) Profiles across the HF and CF showing the distribution of creep rates from north (top) to south using the fault-parallel (N31 W) InSAR velocities. The map in the center shows the location of the profiles, the labeled AAs have their time series shown in Figure 6. The junction between the HF and CF is located near the cyan profile.

velocity field. The time span of the data used to produce the vertical and horizontal velocity maps varies from 2003–2011 (track 206) to 1995–2011 (track 478 frame 747) (supporting information Table S1). Not all the faults have exactly the same strike; the HF is oriented N35°W, the north CF strikes N27°W, and the central CF N30°W (see Figure 13). Because of the small difference in orientation (<8°) we chose to project the horizontal velocity field into motion parallel to the average strike of the HF and CF (N31°W). This orientation is consistent with the maximum shear strain orientation derived from electronic distance measurement data (N31.0°W ± 1.6° for the central and southern San Francisco Bay Area, *Lisowski et al.* [1991]) and with the average strike of the GPS velocities in the Bay Area with respect to LUTZ (Figure 4a, N31.1°W). This confirms that most of the interseismic deformation is fault parallel and follows the averaged N31°W orientation. We additionally validated that the fault-parallel mean velocity map leads to correct estimation of interseismic deformation by comparing with the independent GPS data (Figure 4b), and we verified that it also enables accurate estimation of fault creep by comparing with independent AA data (Figure 5a).

We compared the InSAR fault-parallel velocities with the fault-parallel GPS velocities derived from the horizontal BAVU3 GPS velocities [*Bürgmann et al.*, 2014], both referenced to the centrally located GPS station LUTZ (Figure 4). For the GPS data the uncertainties are shown with 95% confidence level, while for InSAR, as no method currently exist for accurately estimating uncertainties, we use fixed uncertainties of 1.5 mm/yr considering remaining orbital errors and atmospheric noise [*Fattahi and Amelung*, 2014]. We observe a good agreement between the two independent data sets with an average absolute deviation of 2 mm/yr (Figure 4b). The best fit linear regression has a slope of 1.09, which is not significantly different from 1 given the uncertainties. Velocities at pixels with temporal coherence between 0.5 and 0.7 or larger than 0.7 agree equally well with the GPS data, confirming that in the Bay Area a temporal coherence threshold of 0.5 is acceptable (Figure 4b). As InSAR data are relative observations, uncertainties are also relative. The maximum distance between the LUTZ reference station and a GPS station considered in the comparison is ~80 km (supporting information Figure S3). Thus, these

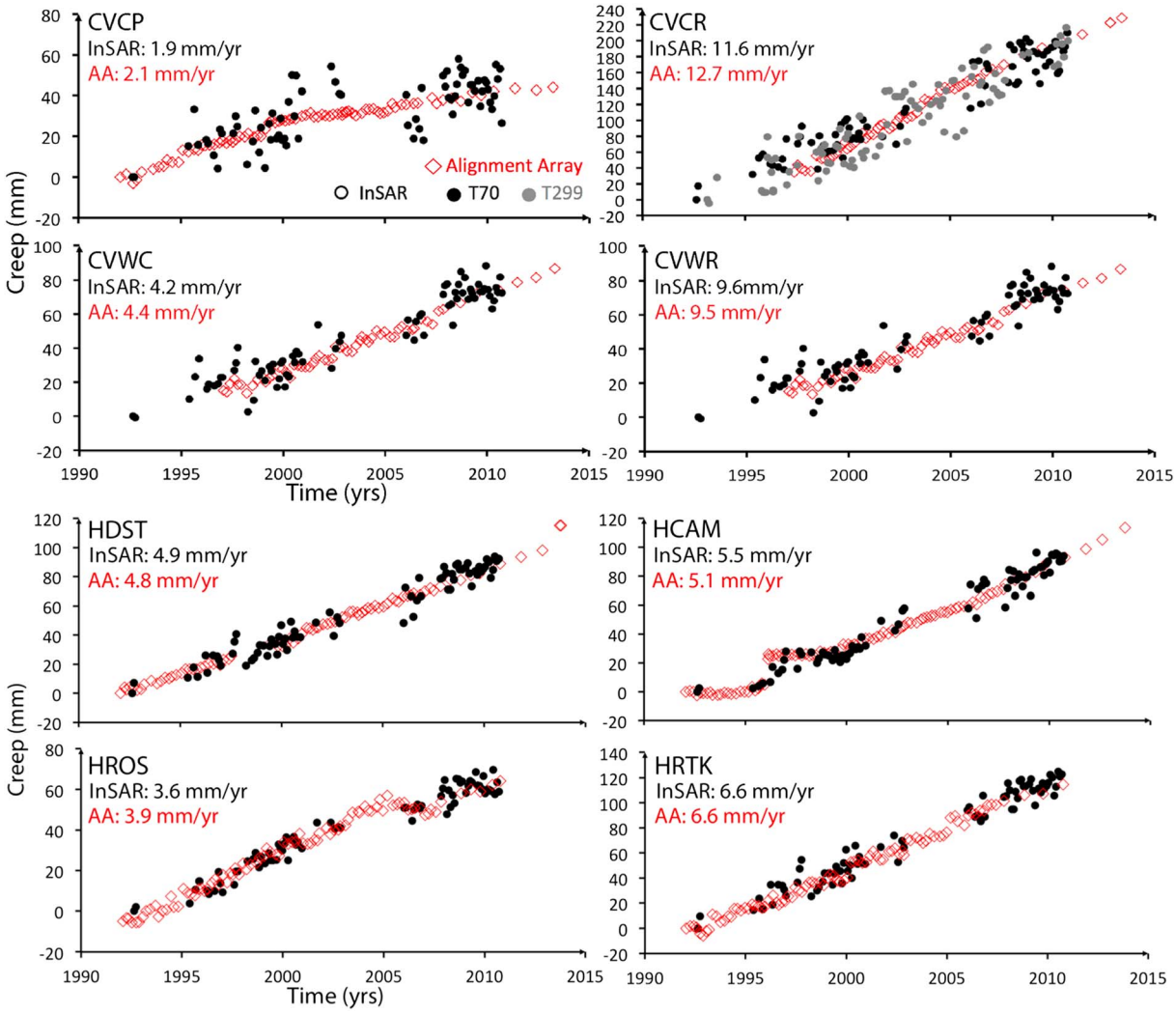

Figure 6. Temporal variability of surface creep on the CF at four AAs, (top) CVCP, CVCR, CVWC, and CVWR and on the HF, (bottom) HDST, HCAM, HROS, HRTK, locations shown in Figures 1 and 5a. The dots show cumulative offsets between clusters of pixels across the faults from the fault-parallel InSAR velocity field (track 70, black, track 299, grey) and the red diamonds show the AA data. The linear creep rates are labeled at the top and agree well between AAs and InSAR. The AA uncertainties are smaller than the marker size and the scatter in the InSAR data illustrate the uncertainties associated with each time step.

results demonstrate that InSAR mean velocity maps enable resolving vertical and horizontal deformation partitioning in the Bay Area for short- and long-wavelengths signals as small as 2 mm/yr over a distance up to 80 km. For the remainder of this paper we use the average absolute deviation (2 mm/yr) between the InSAR and GPS velocities as uncertainties for the InSAR velocities.

2.2.3. Alignment Arrays

Using the mean InSAR fault-parallel velocity map, we produced closely spaced across-fault profiles and estimated the HF and CF creep rates from the detected offset (Figure 5). We observe a good agreement between decadal InSAR surface creep estimates and up to multidecadal AA creep rates (using linear regressions through time) on both CF and HF (Figure 5a). These long-term creep estimates agree within less than ±0.4 mm/yr on the HF (with multidecadal AAs) and within ±1.3 mm/yr on the CF for AAs installed more recently. Because most of the deformation near the HF and CF is horizontal (Figure 1), estimates of creep rates from the descending-only InSAR mean velocities projected into fault-parallel orientation would give comparable results, the exception being near San Jose where significant vertical motion occur in the Santa Clara Valley leading to overestimation of the creep rates from the descending mean velocity field (Figure 1). For this reason it is preferable to use the fault-parallel motion rather than LOS velocities to avoid inclusion of vertical deformation associated with hydrologic and tectonic processes. Given the good agreement between

the InSAR mean velocities derived from motion parallel to the average strike of the HF and CF (N31°W) and the independent GPS (Figure 4b) and AA data (Figure 5a), we confirm that the consideration of the average-fault-parallel motion does not introduce significant bias and thus can be used for modeling fault slip rates.

We compared time series of estimates of cumulative surface creep on the CF and HF obtained from InSAR with AA measurements at eight sites [*Lienkaemper et al*., 2014] (Figure 6). We generated time series by calculating the difference in cumulative displacement for pixels comprised in boxes of 200 × 200 m on both sides of the fault at the locations of the AAs for each InSAR acquisition time [*Lanari et al*., 2007]. We confirm a good agreement between the long-term creep rates (0.1 to 1.1 mm/yr) but notice a significant scatter in the InSAR time series (Figure 6), the scatter being larger for sites on the CF than on the HF. This temporal scatter can either be due to atmospheric noise, which has a low contribution in the mean velocity maps but is nonnegligible in individual time steps, or to soil processes (soil moisture and vegetation changes) explaining the larger scatter associated with the CF near vegetated hillsides. This larger scatter relates to the lower temporal coherence of pixels near the CF (~0.6) compared to pixels near the HF with temporal coherence of ~0.9–1.0 (Figure 2), suggesting that future works focusing on time-dependent deformation should use a higher temporal coherence threshold. Given the observed scatter and the observation that the creep rates are mostly linear between 1992 and 2011 (Figure 8), this study utilizes the mean velocity field and does not consider time-dependent modeling [*Shirzaei and Bürgmann*, 2013].

3. Results

3.1. Vertical and Horizontal Deformation in the Bay Area

The decomposition of LOS InSAR into vertical and horizontal motions (Figure 1) confirms that most of the interseismic deformation in the Bay Area is horizontal (i.e., mostly tectonic), the vertical deformation being mostly local. The horizontal deformation can be separated into two components: the long-wavelength deformation resulting from interseismic elastic strain accumulation along locked faults of the San Andreas Fault (SAF) system, and the short-wavelength deformation (near fault) marked by sharp gradients in displacement observed across the HF and the CF that reflect shallow creep (Figure 1, left).

The vertical deformation in the Bay Area is mostly localized and associated with hydrological effects (Figure 1, right). Subsidence along the shorelines and floodplains south of San Francisco has been described by *Ferretti et al*. [2004] and relates to compaction occurring in manmade fill and Bay mud rich in clays. Uplift in the Santa Clara Valley, near San Jose, has been described by *Chaussard et al*. [2014] and relates to long-term recovery of the aquitards following the pre-1965 groundwater drawdowns. Another localized subsidence signal is observed near Dublin and Livermore also associated with groundwater withdrawal. The only vertical signal potentially related to tectonic deformation is the uplift at 0.5–1 mm/yr observed in the East Bay Hills (between the HF and northern CF) (see supporting information Figure S4 for saturated color scale). This rate of deformation is below our confidence threshold of 2 mm/yr and could be either associated with atmospheric noise in these higher-elevation areas bounded by the faults, or related to tectonic uplift of the Mission Hills [*Bürgmann et al*., 2006]. These uplift rates are consistent with geologic terrace uplift data in Niles Canyon [*Kelson et al*., 1993; *Kelson and Simpson*, 1995] but neither vertical GPS data nor leveling data [*Gilmore*, 1993] allow us to further validate this signal due to the high noise level in the vertical GPS data (supporting information Figure S5) and the potential contribution from hydrological effects in both data sets. Prolonged GPS time series could help confirm the tectonic origin of this signal.

3.2. Surface Creep Distribution on the HCFZ

The high spatial resolution of our horizontal velocity map provides new estimates of surface creep rate variations along the entire length of the HCFZ (Figure 5a). We identify a net increase in creep rate from ~0 ± 2 mm/yr on the northern CF to 10–14 ± 2 mm/yr on the central CF. The transition from the slip being partitioned between the northern CF and HF to slip occurring only on the central CF is clearly marked by a creep rate increase from ~4 ± 2 to 11 ± 2 mm/yr near Alum Rock. Profiles through the HF-CF connection (Figure 5b) illustrate this transfer of surface creep from the HF in the north toward the central CF in the south. The high spatial resolution of the InSAR velocity map also enables us to isolate the southernmost occurrence of creep on the HF, located ~15 km farther south than prior determinations based on AA data and field mapping [*Chaussard et al*., 2015].

3.3. Subsurface Slip Distribution on the HCFZ

We aim to resolve detailed slip at shallow depths relying on the high spatial resolution of the InSAR data and chose to invert for slip rates below and above the locking depths independently. Because the Green's functions adapted to resolve detailed shallow slip have increasingly limited resolution for depths larger than 7.5 km, as shown by a checkerboard test (supporting information Figure S6), using a simultaneous inversion to resolve shallow and deep slip rates would result in large uncertainties at depths even if using larger elements. Instead, we chose to perform independent inversions and acknowledge the existence of trade-offs between the long-term slip rates and the creep rates near the locking depth. An alternative approach would be to combine two Green's functions in a simultaneous inversion and setting slip rate bounds depending on the depth, but we prefer avoiding the addition of constraints to our model. Another possibility would be a joint inversion for a block model involving rotations of fault-bounded blocks and shallow distributed slip [*Evans et al*., 2012], which neglect vertical motion but would be interesting to pursue in future work with regional InSAR data.

To constraint the deep slip, measurements need to be made at significant distances from the faults to capture the full interseismic deformation, preferably to five times the locking depth (90% of total deformation is within ~60 km, assuming a 12.5 km locking depth [*Savage and Burford*, 1973]). Thus the far-field deformation reflects the long-term slip at depth, while the near-field data contains minimal information about the long-term slip rates. On the other hand the near-field deformation reflects the shallow slip due to creep often measured within a few hundreds of meters of the fault with AAs. Accordingly, we separate the deformation field so the long-term slip is mostly constrained by the far-field deformation and the shallow slip by the near-field deformation. The locking depth is fixed to 12.5 km, which is relatively well constrained based on seismicity [*Waldhauser and Ellsworth*, 2002], has been studied in further detail in previous works [e.g., *d'Alessio et al*. [2005]; *Field et al*. [2015]] and has a minimal influence on the shallow slip rates estimates.

3.3.1. Long-Term Slip Rates

We invert the long-wavelength InSAR velocity field (strain accumulation) for long-term slip rates (loading rates) on deep dislocations (below locking depths) [*Bürgmann et al*., 2006]. We mask the near-fault velocity field corresponding to creep (areas within a horizontal distance of one locking depth from the faults). We invert for slip rates on 3000 km deep vertical faults to approximate screw dislocations to infinite depth [*Savage and Burford*, 1973], following the Bay Area fault geometry of *Bürgmann et al*. [2006]. The model and data agree well (Figure 7, top row) with a Weighted Residual Sum of Squares (WRSS) of ~2.6 mm/yr on the unmasked far-field residuals (difference between model and data used in the inversion, not considering the near-fault deformation) and ~5.5 mm/yr on the total residuals (removing the mask from the near-fault a area), the only systematic residuals corresponding to the near-fault areas affected by shallow creep on the HF and CF. The slip rate uncertainties are directly dependent on the InSAR mean velocity uncertainties and are fixed at 2 mm/yr (after validation with the independent GPS data, Figure 4), which is likely a lower bound estimate but is on the same order as the GPS and geological slip rate uncertainties.

We compare inversions based on InSAR (Figure 7, top row) and on GPS data (Figure 7, bottom row). The modeled long-term slip rates from InSAR are ~22 ± 2 mm/yr on the central CF, 10 ± 2 mm/yr on HF, and 6 ± 2 mm/yr of the northern CF (Table 1). In the GPS-only inversion the SAF has a higher slip rate (21.5 ± 1 compared to 19.5 ± 2 mm/yr), and the central CF has a lower slip rate (19.5 ± 2 compared to 22 ± 1 mm/yr, respectively). Similarly, the only difference between the InSAR-based model and the dislocation model of *Bürgmann et al*. [2006] mostly based on GPS data, is a lower slip rate on the SAF of 19.5 ± 2 mm/yr (Table 1). However, these differences are small, which demonstrates that the InSAR mean velocity field provides sufficient constraints to the deep dislocation model and the addition of GPS data does not provide additional constraints in the inversion. For a joint inversion, analysis of optimal weighting of the two data sets is necessary and would require in depth investigation given the large difference in number of data points and covariance, which is not the focus of this paper.

Geological estimates suggest rates of 15 ± 3 mm/yr on the central CF, 9 ± 2 mm/yr on the HF, and 6 ± 2 mm/yr on the northern CF [*Field et al*., 2015]. Estimates derived from published block models of GPS velocities include rates of 12.4–17.6 ± 2.6 mm/yr on the central CF, of 6.5–7.6 ± 1.4 mm/yr on the HF, and of 4.2–10.0 ± 1.6 mm/yr on the northern CF from *d'Alessio et al*. [2005], rates of 11–16 mm/yr on the central CF, of 7–9 mm/yr on the HF, and of 3–8 mm/yr on the northern CF from *Johnson and Fukuda* [2010], and rates of 15.6 ± 0.8 mm/yr on the central CF, of 6.7 ± 0.8 mm/yr on the HF, and of 9.0 ± 0.9 mm/yr on the northern CF

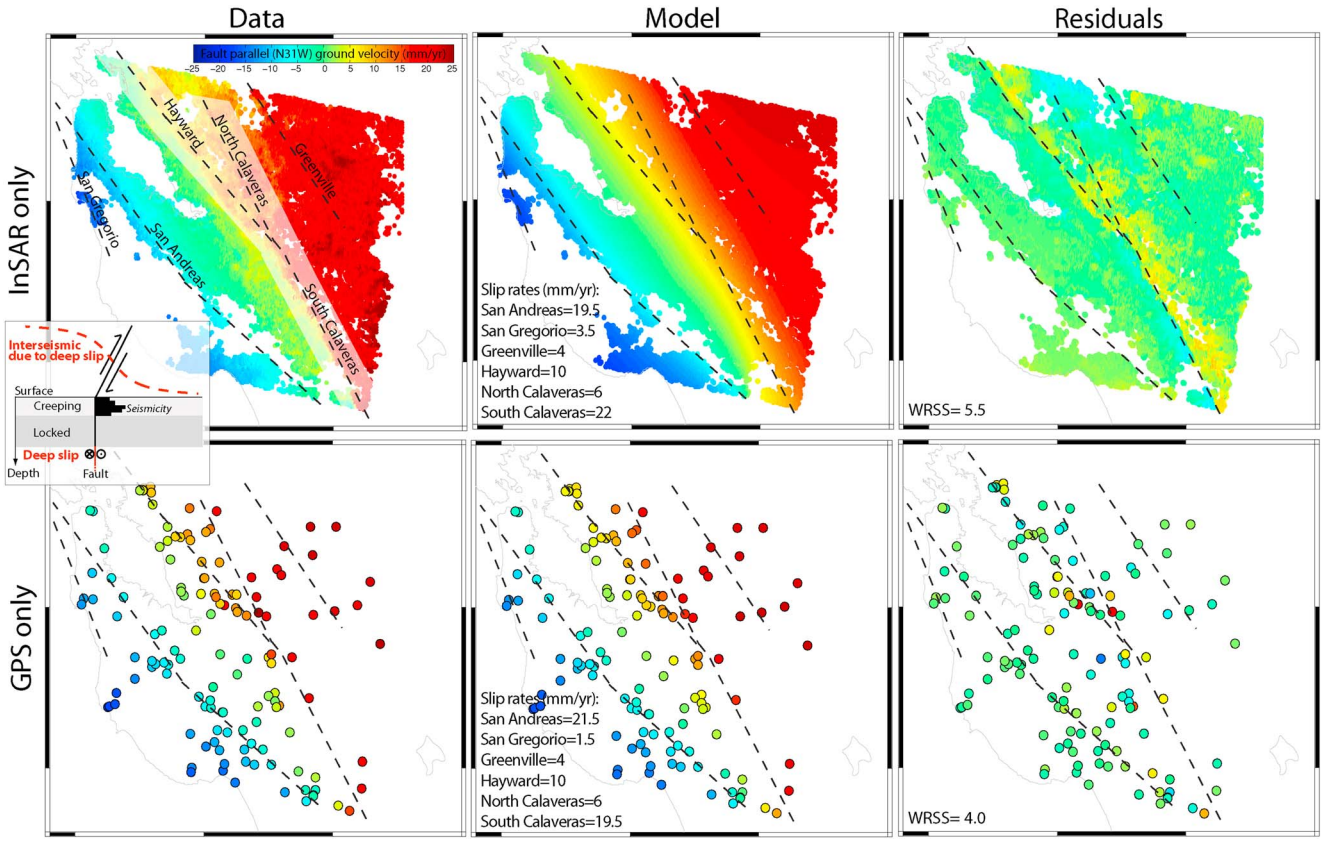

Figure 7. Deep dislocation model. The dashed lines indicate the surface projection of the 3000 km deep vertical dislocations, based on *Bürgmann et al.* [2006]. The inversion (top row) based on InSAR only and (bottom row) based on GPS only. The first column shows the data, the second the model, and the last column shows the residuals (difference between data and model). The near-fault velocity field (areas within a horizontal distance of one locking depth from the faults, white overlay on the InSAR data) is masked for the inversion but shown in the residuals. This residual velocity field, dominated by deformation due to shallow fault creep is used for the inversion of slip rates above the locking depth (Figure 8).

from *Evans et al.* [2012] (Table 1). The slip rate estimated on the central CF is slightly higher using deep dislocation models than relying on block models or geological data, but these differences are small and within the range of uncertainties associated with these models.

3.3.2. Shallow Slip Rates From Creep

Shallow slip rates (above the locking depth of 12.5 km) are inverted from the InSAR fault-parallel motion corrected for the deformation from the deep dislocation model (i.e., inversion of the residuals shown in Figure 7). We use the geometry of the HCFZ presented by *Chaussard et al.* [2015] to build a triangular mesh of the fault system and perform a least squares inversion of the residuals from the deep slip model with smoothness and positivity constraints to estimate the fault slip rates from the geodetic data. We calculate the displacements due to uniform slip on each triangular dislocation element in a homogeneous elastic half-space [*Okada*, 1985] following *Meade* [2007]. A smoothing constraint is imposed using a Laplacian operator implemented from *Resor* [2003]. The effect of the Laplacian operator is to decrease the variation of slip between neighboring

Table 1. Dislocation Model Strike-Slip Rates (in mm/yr) From the InSAR-Only Inversion (InSAR) Compared to Results From the GPS-Only Inversion (GPS) and Results From *Bürgmann et al.* [2006] (GPS-SAR) Who Followed the Same Modeling Approach but Aligned the InSAR Velocity Field to GPS Data, Results From *d'Alessio et al.* [2005] Who Used a Block Model (Block), and Geological Slip Rates Estimates (Geol) of *Field et al.* [2015]

	SG (mm/yr)	±	SAF	±	HF	±	CF N	±	G	±	SAF SCM	±	CF C	±
InSAR	3.5	2	19.5	2	10	2	6	2	4	2	19.5	2	22	2
GPS	3.5	1	21.5	1	10	2	6	2	4	2	21.5	1	22	1
GPS-SAR	3.5	1	21.5	2	10.3	2	5.9	2	3.8	2	19.5	1	22.8	1
Block	2.6–5.1	1	16–17.1	2	6.5–7.6	1	4.2–10	2	0–6.2	2	13–16.4	2	12.4–17.1	3
Geol	3	2	17	4	9	2	6	2	3	1	17	4	15	3

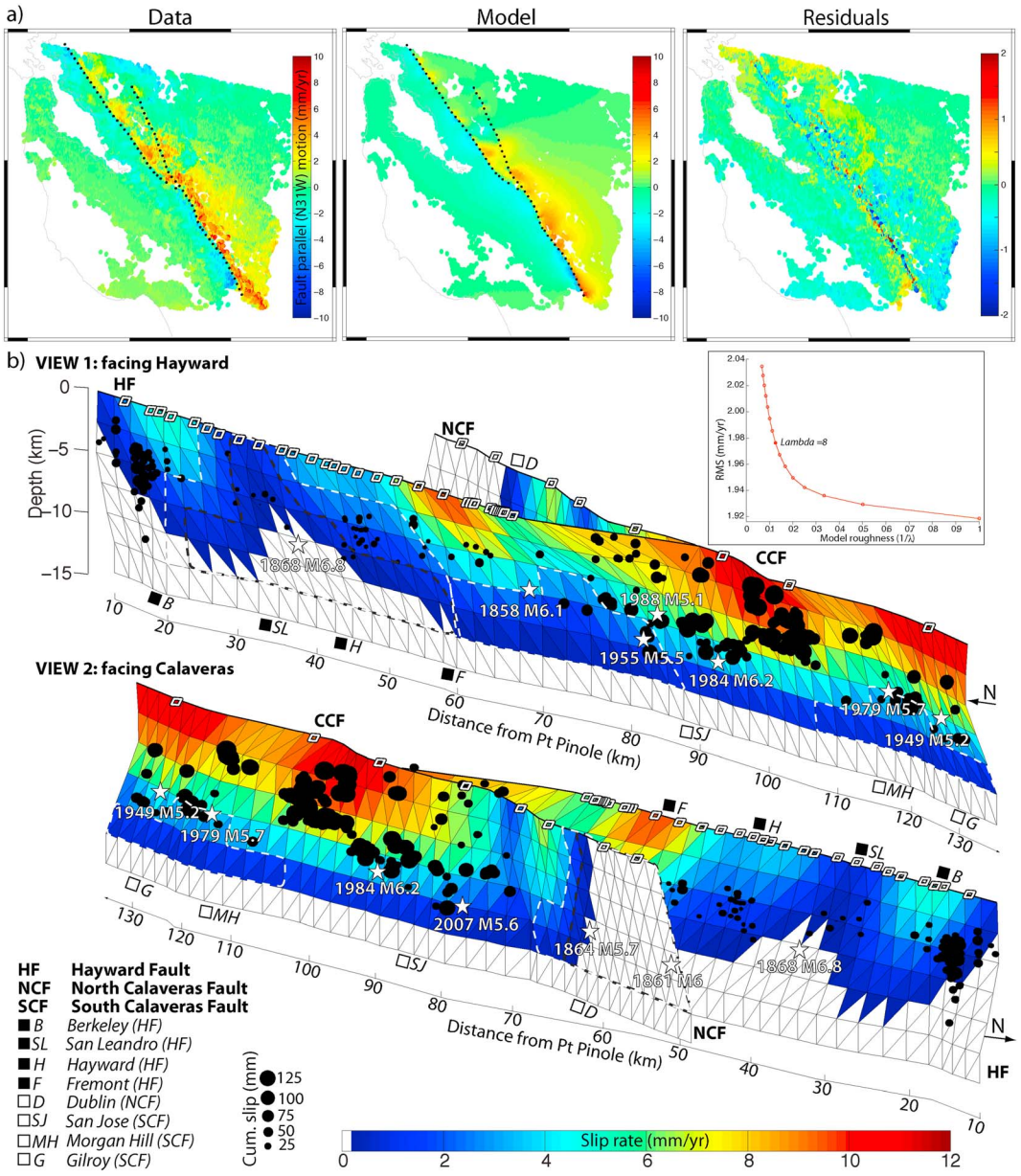

Figure 8. (a) Mean velocity maps produced by the shallow slip model (model, Figure 8b) inverted from InSAR fault-parallel motion corrected for the deformation from the deep dislocation model (data) and difference between the two (residuals). (b) Shallow slip rates distribution (above locking depth) on the HCFZ. In the top view north is toward the left (facing HF); in the bottom view north is toward the right (facing CF). Black dots are CREs with their size proportional to 1992–2011 cumulative slip, white stars are historical earthquake locations, and white diamonds show the AA locations. The black dashed lines highlight locked patches (<1 mm/yr) and the white dashed lines low slipping patches (<3 mm/yr). The top right inset shows the RMS as a function of model roughness (inverse of the Laplacian smoothing factor).

patches by smoothing it across common edges of triangular elements. Thus, increasing the smoothing increases model misfit. The strength of the smoothing is determined by visual inspection of the trade-off (Tikhonov) curve between model misfit (quantified using a root-mean-square (RMS)) and model roughness (inverse of the Laplacian operator) [e.g., *Du et al*., 1992] and by finding the best agreement between the produced slip rates on surface patches and the measured slip rates at AAs.

The slip rates distribution of the preferred model (Laplacian smoothing factor of 8) is shown in Figure 8b (see supporting information Figure S7 for models with lower and higher smoothing factors) and its corresponding

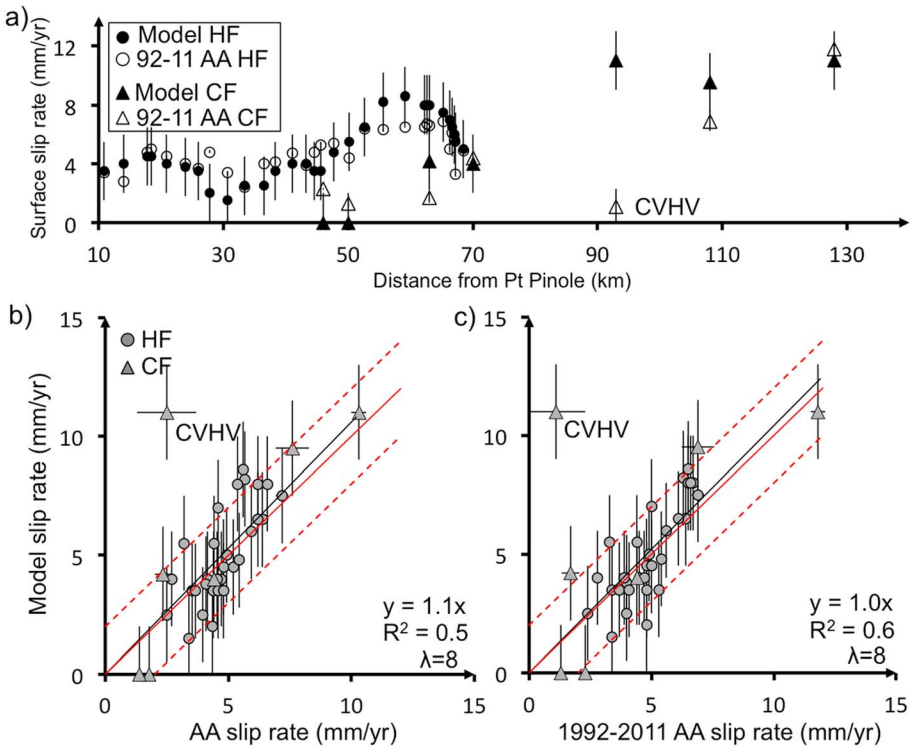

Figure 9. Comparison between slip rates produced by the model at the locations of the HF AAs (dots) and the CF AAs (triangles) and the AA detected surface creep. Uncertainties for the modeled slip rate are fixed to 2 mm/yr, which correspond to the uncertainties of the InSAR mean velocities. (a) Modeled surface slip rates (black) and 1992–2011 AA creep (white) as a function of the distance from Point Pinole (km). (b) Modeled surface slip rates versus AA surface creep considering AA data for the full available time period. (c) Same as Figure 9b but considering linear regression on AA data between 1992 and 2011 (or a subset of this time period depending on availability at each site). The full red line shows a 1 to 1 linear regression and the two dashed red lines ±2 mm/yr deviation (confidence level of the InSAR data). The black line shows the best fitting linear regression with the parameters shown in the bottom right. The CVHV AA is an outlier because it encompasses only one strand of the central CF (J. Lienkaemper, personal communication, 2015). Similar figures for higher and lower Laplacian smoothing operators (λ) are shown in the supporting information Figure S8.

fit to the data is shown in Figure 8a. No uncertainties are estimated from this model as the result depends on the smoothing factor but the model uncertainties are directly dependent on the InSAR mean velocity uncertainties (2 mm/yr). The preferred model provides a good fit to the data, a relatively low RMS of 1.97 mm/yr (used as uncertainties in Figure 10b) and shows the best agreement between slip rates on near surface patches and creep rates observed by AAs on the HF and CF (Figure 9). The agreement is further improved when considering only 1992–2011 AA data (Figure 9, see supporting information Figure S8 for equivalent figures for lower and higher smoothing factors models). The view from the southwest facing the HF (Figure 8b, top) reveals similar features to previous models of the HF: a slow creeping patch near Berkeley (~3 mm/yr), a locked patch beneath San Leandro, and a fast creeping patch near Fremont (~9 mm/yr) [*Schmidt et al*., 2005; *Shirzaei and Bürgmann*, 2013]. The view from the southeast facing the CF (Figure 8b, bottom) reveals a locked patch on the northern CF north of Dublin, a slow creeping patch south of Dublin (~3 mm/yr), and two fast creeping patches on the central CF (>12 mm/yr) south of San Jose and south of Morgan Hill, separated by a slower patch (~9 mm/yr). Most of the aseismic slip is limited to the shallowest 5 km on both the HF and the CF. This suggests partial to full locking at depths of 5 to 12.5 km in agreement with the locations of historical earthquakes (Figure 8b) and with the locked patches proposed by *Oppenheimer et al*. [1990] based on the distribution of microseismicity on the fault.

Microseismicity along the HCFZ includes characteristically repeating earthquakes (CREs) [*Bürgmann et al*., 2000; *Peng et al*., 2005; *Templeton et al*., 2009; *Chaussard et al*., 2015] (Figure 8b), which are events that occur in near identical locations, with similar magnitudes, and with high waveform correlation coefficients (>0.95)

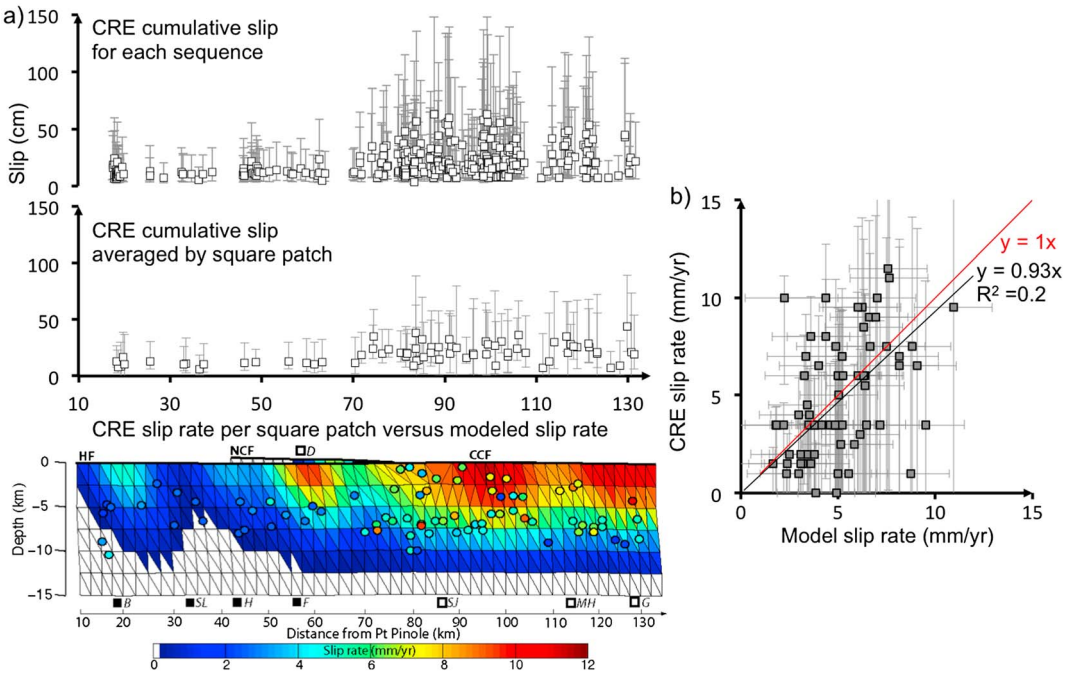

Figure 10. Comparison between modeled slip rates and CRE slip rates. (a) CRE cumulative slip as a function of the distance along the fault for all the events, the grey lines show the error bars (top); same as Figure 10a but for CRE cumulative slip averaged over square patches (2.5 km along fault and 2.5 km in depth) (middle); and CRE slip rates averaged over square patches compared to the modeled slip rates (inverted from the InSAR-derived deformation) with same color scale (bottom). (b) Comparison between CREs slip rates and modeled slip rates both averaged over square patches. The red line shows a 1 to 1 linear regression and the black line shows the best fitting linear regression.

[*Nadeau and Johnson*, 1998]. CREs are believed to represent locked asperities that are loaded by the surrounding aseismic creep and rupture repeatedly. Fault slip parameters are calculated from the scaling between recurrence time, seismic moment, and slip of CREs [e.g., *Chen et al*., 2007], first established at Parkfield [*Nadeau and Johnson*, 1998]. The CRE locations are estimated using the Double-Difference Real-Time catalog [*Waldhauser and Schaff*, 2008] and the cumulative displacement is calculated from the empirical relationship between seismic moment and slip [*Nadeau and Johnson*, 1998; *Chen et al*., 2007] (see *Chaussard et al*. [2015] for details). We compare the InSAR-inverted HCFZ slip distribution with the CRE locations and their 1992–2011 cumulative displacements (Figures 8b and 10). We observe a good spatial agreement between the locations of CREs and the locations of slipping patches (Figure 8b). The majority of the CREs are located on the central CF near the rapidly creeping patches (red in Figure 8b). The northern CF is not associated with any clear CRE sequences, in agreement with its low creep rate ($<$4 mm/yr in the south and episodic and $<$2 mm/yr in the north, white and blue colors in Figure 8b). The majority of the CREs on the HF are located in the vicinity of the Berkeley and the Fremont creeping patches (Figure 8b).

Figure 10a shows the cumulative slip from the CREs between 1992 and 2011 for all sequences (top) and averaged over square patches of 2.5 $\times$ 2.5 km (middle). The CRE uncertainties are evaluated based on the recurrence intervals after deriving a relationship from the 1984–1998 Parkfield catalog that was used to obtain the scaling equation [*Nadeau and Johnson*, 1998]. The cumulative slip has large and asymmetric uncertainties because the scaling relationship is defined in a log space. The bottom panel of Figure 10a shows the slip rate from the CREs averaged over square patches color coded in the same way as the slip rate from the modeled shallow slip rates inverted from the InSAR data. The CREs support a clear difference in creep rates between the HF and the central CF, the CREs on the HF being significantly scarcer and having lower slip rates (Figure 10a). Figure 10b shows the slip rates from the CREs versus the modeled slip rates both averaged over square patches. There is an acceptable agreement between the CRE and the modeled slip rates, the correlation of coefficient is low (0.2) but no systematic bias is observed, confirming that the scaling of CRE-derived slip established at Parkfield [*Nadeau and Johnson*, 1998] can be used on other faults.

4. Discussion

4.1. Distribution of Locked and Creeping Patches

The distribution of locked and creeping patches from the InSAR inversion reveals similar features highlighted by prior works on the HF relying on AAs, GPS, CREs, and InSAR data or a combination of these techniques [*Simpson et al*., 2001; *Malservisi et al*., 2003; *Schmidt et al*., 2005; *Lienkaemper et al*., 2012; *Shirzaei and Bürgmann*, 2013]: the slow creeping patch near Berkeley, the locked patch beneath San Leandro, and the fast creeping patch near Fremont, extending further south given the revised geometry of *Chaussard et al*. [2015]. The only work suggesting a significantly different distribution of locked and slipping patches on the HF is *Evans et al*. [2012] who find the strongest coupled patches at shallow depths south of Berkeley, near Hayward, and south of Fremont. We consider this distribution unlikely given the significant amount of surface creep observed in the InSAR data in these areas. On the central CF *Oppenheimer et al*. [1990] and *Oppenheimer and Lindh* [1992] identify five areas lacking microseismicity interpreted as locked patches, most of which failed during historic earthquakes. *Manaker et al*. [2003] show that models derived from trilateration and GPS data agree with the locations of these locked areas. Our model of the central CF shows that creep along most of the fault is located at depths shallower than 5 km arguing that locked patches exist in the locations of the microseismicity voids, in agreement with these works. This slip distribution also agrees with geodetic rupture models suggesting the presence of locked zones at depths $>$5 km [*Du and Aydin*, 1993] and with the distribution of slip of the Morgan Hill earthquake, for which the coseismic slip occurred at depth (in locked sections) and the shallow slip deficit was reduced through afterslip [*Templeton et al*., 2009]. Additionally, our model suggests locking of most of the northern CF, supported by the lack of seismicity and CREs, but this segment has not been studied in depth by other works.

The slip behavior is believed to be controlled by the stiffness of surrounding rocks and the frictional fault surface and gouge properties [*Marone and Scholz*, 1988], creeping patches reflecting velocity-strengthening conditions [*Marone*, 1998]. In major fault zones worldwide, the locations of creeping patches have been related to the occurrence of weak minerals such as ophiolite bodies on the North Anatolian Fault [*Cetin et al*., 2014], and weak clay minerals on the creeping strand of the San Andreas Fault [*Schleicher et al*., 2010; *Carpenter et al*., 2011; *Lockner et al*., 2011] and in Taiwan [*Lee et al*., 2003]. The HF internal structure has been studied based on microseismicity [*Waldhauser and Ellsworth*, 2000; *Zhang and Thurber*, 2003] and geological mapping [*Moore and Ponce*, 2001; *Ponce et al*., 2003], leading to the development of a 3-D geologic model [*Jachens et al*., 2003; *Graymer et al*., 2005]. Because our distribution of slip on the HF agrees with previous works, the parameters formerly suggested as influencing the location of creeping and locked patches (distribution of mafic bodies [*Ponce et al*., 1998; *Waldhauser and Ellsworth*, 2000]) can explain our observations. An alternative control on the slip behavior is the local stress field [*Rivera and Kanamori*, 2002], creep occurring on fault sections with low normal stress [*Argus and Gordon*, 2001] and elevated pore fluid pressures, which act to decrease the effective normal stress on the fault. Additionally, *Hardebeck and Aron* [2009] showed that high stress drops do not directly correlate with the strength of the wall rock. Thus, the relationship between fault creep, stress, and strength of the wall rock remains uncertain.

The geology of the central and northern CF, for which we provide refined slip distribution estimates, has not been precisely constrained, making evaluation of the factors responsible for the distribution of creeping and locked patches difficult. The sedimentary rocks of the Evergreen Basin, composed in great part of clays, overlaying Franciscan bedrock at 3–5 km depth [*Koltermann and Gorelick*, 1992; *Wilson and Gorelick*, 1996; *Jachens et al*., 2002; *Williams et al*., 2002; *Boatwright et al*., 2004; *Ponce et al*., 2005; *Watt et al*., 2007] could provide the conditions for creep on much of the shallow portion of the central CF [*Sieh and Williams*, 1990]. However, the limited creep on the northern CF despite the existence of similar deposits in the Livermore basin [*California Department of Water Resources*, 1980] may argue for a more complicated control on the slip behavior. The change in geometry from the north to the central CF, near 37°24′N (change in strike from ~N27°W to ~N30°W) would argue for a higher creep potential on the more northerly striking northern CF due to a lower level of normal stress [*Argus and Gordon*, 2001]. However, the lower amount of surface creep on the northern CF compared to the central CF suggests that the local stress field may not play a dominant role in the distribution of creep [*Bilham and Williams*, 1985]. The existence of a sharp material interface across the CF marked by a net contrast in velocity south of N37°28′ [*Zhao and Peng*, 2008] could suggest that the larger creep along the central CF compared to the northern CF is related to compositional effects. Multiple factors likely lead to the observed aseismic fault slip behavior, thus

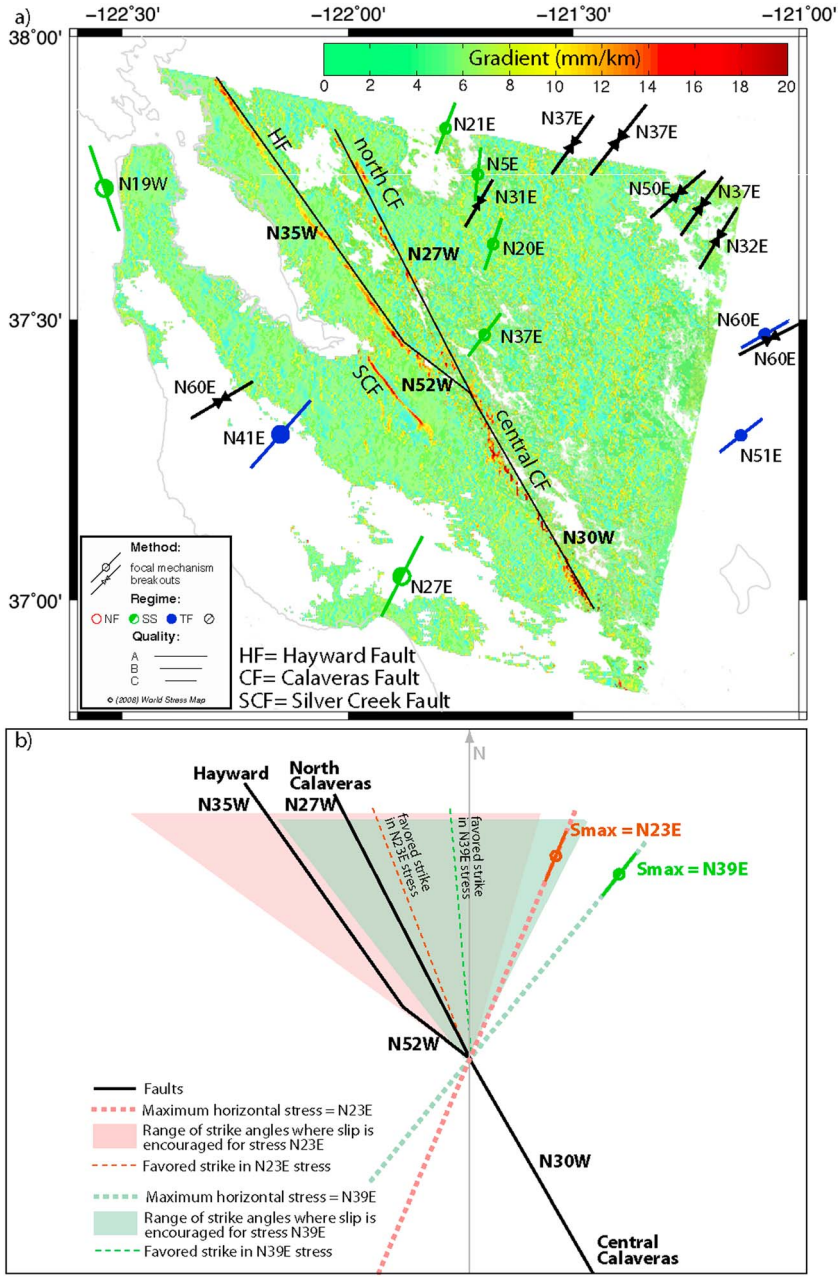

Figure 11. (a) Gradient map from *Chaussard et al.* [2015] calculated from the InSAR mean ground velocity in the fault-perpendicular direction and regional stress orientation (World Stress Map data [*Heidbach et al.*, 2008]). High gradient (red) show creeping faults surface traces (HF and CF, black lines) and the Silver Creek Fault, which blocks groundwater flow in the Santa Clara Valley aquifer [*Chaussard et al.*, 2014]. (b) Range of strike angles for which slip would be encouraged for a rupture propagating northward on the central CF considering two stress scenarios: N23°E, in red, and N39°E, in green. The strike of the northern CF of is more favorable for rupture propagation than the HF.

improved geologic and structural models of the central and northern CF are necessary to better constrain the first-order controls on this process.

4.2. Slip Partitioning in the East San Francisco Bay

Our refined estimation of slip partitioning in the East Bay can help identify the dominant tectonic structures. The long-term slip rates estimated from modeling of the long-wavelength InSAR velocity field, from block modeling [*d'Alessio et al.*, 2005] and from geology [*Field et al.*, 2015] all agree that the HF slip rate is larger than

the northern CF slip rate (Table 1). This observation suggests that most of the tectonic deformation is accounted for by the HF (~60%) in the northern East Bay. It is believed that the Evergreen fault was the southern extension of the HF and that slip later jumped from the Evergreen fault eastward to the central CF [*McLaughlin et al*., 1996; *Jachens et al*., 2002]. In this perspective the HF would have been the dominant structure in the East Bay and the central CF became its southern extension. This interpretation suggests a direct continuity between slip on the HF and central CF, which is also supported by the distribution of the CREs. Therefore, the continuous HF and the central CF appear to be the structures accommodating the majority of the slip in the East Bay, in agreement with the long-term estimates of cumulative offset of at least 174 km on the HF and CF since ~12 Ma [*McLaughlin et al*., 1996; *Wakabayashi*, 1999].

The direct connection between the HF and central CF at depth and along the surface [*Chaussard et al*., 2015] enables potential earthquake ruptures involving both faults. A rupture nucleating on the HF could propagate southward along the central CF, producing a much larger earthquake. Alternatively, a rupture nucleating on the central CF could either propagate northward onto the HF or along the northern CF. From a geometrical perspective the central CF bifurcates into the HF via a northeast dipping fault section through a restraining left bend, while its connection with the more northerly striking northern CF is relatively direct. We calculate the range of strike angles for which slip would be encouraged for a rupture propagating northward on the central CF using the Coulomb Failure theory [*Bhat et al*., 2004; *Oglesby*, 2005] given the regional stress orientation (N23–39°E, World Stress Map data [*Heidbach et al*., 2008]) and compare these angles to the surface traces of the HF and northern CF using a gradient map of the mean InSAR horizontal velocity [*Chaussard et al*., 2015] (Figure 11a). When considering a regional stress orientation of N23°E both the HF and the northern CF fall in the range of strike angles for which slip would be encouraged (Figure 11b, red area), while when considering a regional stress orientation of N39°E only the northern CF falls in the range where slip would be encouraged (Figure 11b, green area).

In both cases we find that geometrically the northern CF strike is more favorable for rupture propagation than the HF given the regional stress orientation (Figure 11b). Additionally, the northern CF is more fully coupled than the HF and could thus be the preferential path for a rupture propagating from the central CF. However, *Schwartz et al*. [2012] also propose that differences in the accumulated strain exert a strong control on fault branching. Considering the time since the last earthquakes, the long-term slip rates, and the amount of surface creep we evaluate that the moment magnitude deficit is larger on the HF (*M*6.9) than on the northern CF (*M*6.6) (see section 4.3). Thus, in this perspective, the HF could be a more likely path for propagation of a rupture from the central CF. Models of rupture propagation integrating the refined 3-D geometry of the faults connection [*Chaussard et al*., 2015], our refined distribution of slip rates on the faults, and consideration of different rupture velocities should be performed to improve earthquake rupture propagation scenarios in the East Bay [e.g., *Lozos et al*., 2014].

4.3. Moment Magnitude Deficit

We consider the slip-predictable approach to evaluate the seismic moment deficit and the potential magnitude of future earthquakes based on the long-term slip rate and elapsed time since the most recent event [*Shimazaki and Nakata*, 1980]. Even though this approach is not fully reliable [*Murray and Segall*, 2002], it allows for a direct consideration of spatial variations in creep rates [*Murray and Langbein*, 2006], the seismic moment deficit being smaller in regions creeping at rates close to the long-term slip rate. We calculate the seismic moment deficit associated with each of the locked and slow creeping patches identified in our model of shallow slip distribution (Figure 8b). The slip-predictable approach considers that the seismic moment deficit on locked patches is equal to the product of the fault area, the shear modulus of the surrounding rock (taken as 30 GPa), the long-term slip rate, and the elapsed time since the most recent event. The most recent events are shown in Figure 8 (white stars) and correspond from north to south along the HF to the 1868 Hayward *M*6.8 [*Lienkaemper et al*., 1991; *Yu and Segall*, 1996; *Toppozada and Borchardt*, 1998], the 1858 *M*6.1, the 1955 *M*5.5, and the 1988 *M*5.1 event [*Oppenheimer et al*., 1990], and on the CF to the 1862 *M*6, the 1864 *M*5.7 [*Oppenheimer et al*., 1990], the 2007 Alum Rock *M*5.6 [*Oppenheimer et al*., 2010], the 1984 Morgan Hill *M*6.2 [*Hartzell and Heaton*, 1986; *Oppenheimer et al*., 1988; *Templeton et al*., 2009], the 1979 Coyote Lake *M*5.7 [*Oppenheimer et al*., 1990; *Simpson et al*., 1999; *Manaker et al*., 2003], and the 1949 Gilroy *M*5.2 event [*Oppenheimer et al*., 1990]. The fully locked patches (model slip $<$1 mm/yr, black dash lines on Figure 8b) are capable of producing a *M*6.7 on the HF near San Leandro (or *M*6.6 considering the long-term geological slip rate rather than the geodetic slip rate

inverted from the long-wavelength InSAR velocity field) and a *M*6.5 on the northern CF, north of Dublin. The low slipping patches (1–3 mm/yr, white dash lines on Figure 8b) are capable of a *M*6.8 on the HF near San Leandro (for both geologic and geodetic slip rates), a *M*6.6 on the northern CF, north of Dublin, a *M*6.5 on the HF, south of Fremont, and of a *M*6.2 on the central CF near Morgan Hill (or *M*6.1 considering the long-term geological slip rate). These estimates are based on locking depth of 12.5 km. If locking depths were to be shallower (e.g., 10 km depth), the magnitude evaluated would decrease by ~0.1.

We additionally evaluate, following the same approach, the moment magnitude deficit for entire fault segments. On creeping patches the slip-predictable approach considers the product of the difference between the long-term slip rate and the creep rate and the elapsed time since the most recent event. Our estimates of the moment magnitude deficit correspond to upper bound values because they consider that the creeping patches would slip to catch up with long-term slip rates during an earthquake [*Noda and Lapusta*, 2013]. Instead of slipping coseismically the creeping patches could slip in the postseismic period as suggested by the significant amount of afterslip observed following certain earthquakes on creeping faults (the San Andreas Fault at Parkfield [e.g., *Johnson et al*., 2006] and the CF near Morgan Hill [e.g., *Murray-Moraleda and Simpson*, 2009]). However, a multisegment rupture scenario involving the creeping patches cannot be ruled out.

We find that to this day the HF could produce a *M*6.9 with a rupture from Berkeley to the junction with the CF (larger by 0.1 if considering a rupture all the way north to San Pablo Bay). Assuming that deformation and aseismic slip have been steady since 1868, the current slip deficit approaches 1.4 ± 0.1 m in the inferred rupture zone of the 1868 HF earthquake, which is close to the estimated coseismic slip of 1.9 ± 0.4 m [*Yu and Segall*, 1996]. This confirms that the HF 1868 rupture zone is late in its current earthquake cycle [*Lienkaemper and Williams*, 2007]. Our *M*6.9 estimate is in agreement with *Shirzaei and Bürgmann* [2013] who noted the potential for a *M*6.8 on the 70 km long HF from the San Pablo Bay to Fremont involving the creeping areas. The deeper extent of creep in their model and the missing extension of the HF south of Fremont likely explain the lower estimate. Such a long rupture is reasonable for the HF given that its 1868 earthquake involved a 50 km long segment [*Yu and Segall*, 1996]. We find that the northern CF could produce a *M*6.6 extending from the northernmost mapped trace of the northern CF (near San Ramon) to the junction with the central CF, this scenario being reasonable given that the northern CF is almost fully locked. The central CF could produce a *M*6.9 for a rupture from the junction to Gilroy (*M*6.8 considering long-term geological slip rate rather than the geodetic slip rate), which would be relatively atypical given that the central CF tends to produce moderate earthquakes with substantial afterslip [*Murray-Moraleda and Simpson*, 2009]. And finally, a joint rupture involving the central CF and the HF could produce a *M*7.1 (*M*7.2 for a rupture north of Berkeley to the San Pablo Bay) and a joint rupture involving the central and northern CF could produce a *M*7.0 (*M*6.8 considering long-term geological slip rates rather than the geodetic slip rates). Such large events involving cascading multisegment ruptures should be considered in earthquake modeling and ground motion scenarios to reevaluate the East San Francisco Bay Area seismic hazard.

5. Conclusion

We show that time series analysis of a large SAR data set enables resolving interseismic deformation for short- and long-wavelength signals as small as 2 mm/yr over the Bay area with a high spatial resolution, even in vegetated areas. A comparison between independent InSAR, GPS, and AA data sets shows that the remaining noise results in significant scatter in InSAR time series but is negligible in mean velocity maps.

InSAR enables characterization of along-fault creep rates on the HCFZ with a high spatial resolution, creep varying from $\sim 0 \pm 2$ mm/yr on the northern CF to $\sim 14 \pm 2$ mm/yr on the central CF, the CF reaching its maximum creep rate south of the surface junction with the HF. The long-term slip rates on these faults obtained by inverting the long-wavelength InSAR velocity field agree with estimates obtained relying on dislocation models constrained by GPS data, block models, and geological slip rate estimates. The distribution of shallow aseismic slip obtained by inverting the short-wavelength deformation is also comparable to previous models focused on the HF and provides a refined characterization of the distribution of locked and creeping patches on the newly identified, continuous fault structure involving the HF, the new strand of the HF south of Fremont, and the central CF. We find that the northern CF is mostly locked, explaining the absence of seismicity and CREs, and we estimate that most of the aseismic slip is limited to the shallowest 5 km, suggesting a partial or full locking of the HCFZ at depths of 5–12.5 km.

Considering the time since the last earthquakes and the difference between the long-term slip rates and the shallow aseismic slip, we evaluate that the slow creeping patches near San Leandro could produce a $M6.8 \pm 0.3$, a $M6.6 \pm 0.2$ north of Dublin, a $M6.5 \pm 0.1$ near Fremont, and a $M6.2 \pm 0.2$ near Morgan Hill. Given the direct connection between the HF and CF and the quasi-continuous locking at depths >5 km, we consider the potential for cascading multisegment ruptures. To this day, the HF could produce a $M6.9 \pm 0.1$ from Berkeley to south Fremont, the north CF a $M6.6 \pm 0.1$, the central CF a $M6.9 \pm 0.2$ for a rupture extending southward to Gilroy, and a joint rupture involving the CF and the HF could produce a $M7.1 \pm 0.1$ or larger if propagating north of Berkeley on the HF or south of Gilroy on the CF.

Acknowledgments

We thank the National Aeronautics and Space Administration (NASA) for support through grant NNX12AQ32G and the U.S. Geological Survey National Earthquake Hazards Reduction Program (NEHRP) for support through grants G12AP20096 and G13AP00035. We thank two reviewers and the Associate Editor for their constructive comments, which helped improving the quality of this paper. The ERS and Envisat original data are copyrighted by the European Space Agency and were provided through the WInSAR archive. Waveform data, metadata, and data products for this study were accessed through the Northern California Earthquake Data Center [*NCEDC*, 2014]. Berkeley Seismological Laboratory contribution 2015–11.

References

Argus, D. F., and R. G. Gordon (2001), Present tectonic motion across the Coast Ranges and San Andreas fault system in central California, *Geol. Soc. Am. Bull.*, *113*(12), 1580–1592.

Berardino, P., G. Fornaro, R. Lanari, and E. Sansosti (2002), A new algorithm for surface deformation monitoring based on small baseline differential SAR interferograms, *IEEE Trans. Geosci. Remote Sens.*, *40*(11), 2375–2383, doi:10.1109/TGRS.2002.803792.

Bhat, H. S., R. Dmowska, J. R. Rice, and N. Kame (2004), Dynamic slip transfer from the Denali to Totschunda faults, Alaska: Testing theory for fault branching, *Bull. Seismol. Soc. Am.*, *94*(6), S202–S213.

Bilham, R., and P. Williams (1985), Sawtooth segmentation and deformation processes on the southern San-Andreas Fault, California, *Geophys. Res. Lett.*, *12*(9), 557–560.

Bilham, R., N. Suszek and S. Pinkney (2004). California creepmeters, *Seismol. Res. Letts. 75*, 481–492. [Available at http://cires.colorado.edu/~bilham/creepmeter.file/creepmeters.htm.]

Boatwright, J., L. Blair, R. Catchings, M. Goldman, F. Perosi, and C. Steedman (2004), Using twelve years of USGS refraction lines to cali- brate the Brocher and others (1997) three-dimensional velocity model of the Bay Area U.S. Geol. Surv. Open File Rep., 2004 – 1282, 34 pp.

Bürgmann, R., D. A. Schmidt, R. M. M. Nadeau, M. d'Alessio, E. J. Fielding, D. Manaker, T. V. McEvilly, and M. H. Murray (2000), Earthquake potential along the northern Hayward fault, California, *Science*, *289*(5482), 1178–1182, doi:10.1126/science.289.5482.1178.

Bürgmann, R., G. Hilley, A. Ferretti, and F. Novali (2006), Resolving vertical tectonics in the San Francisco Bay Area from permanent scatterer InSAR and GPS analysis, *Geology*, *34*(3), 221, doi:10.1130/G22064.1.

Bürgmann, R., I. Johanson, and R. Nadeau (2014), Time-dependent creep of the Calaveras fault from 18-years of InSAR, GPS and repeating earthquakes *U.S. Geological Survey*, *National Earthquake Hazard Reduction Program*, *Final Technical Report* G13AP00035, 17 p. [Available at http://earthquake.usgs.gov/research/external/reports/G13AP00035.pdf.]

California Department of Water Resources (1980), Ground water basins in California, *Bulletin 118–80*, January 1980.

Carpenter, B. M., C. Marone, and D. M. Saffer (2011), Weakness of the San Andreas Fault revealed by samples from the active fault zone, *Nat. Geosci.*, *4*(4), 251–254, doi:10.1038/NGEO1089.

Casu, F., M. Manzo, and R. Lanari (2006), A quantitative assessment of the SBAS algorithm performance for surface deformation retrieval from DInSAR data, *Remote Sens. Environ.*, *102*(3–4), 195–210, doi:10.1016/j.rse.2006.01.023.

Cetin, E., Z. Çakir, M. Meghraoui, S. Ergintav, and A. M. Akoglu (2014), Extent and distribution of aseismic slip on the Ismetpaşa segment of the North Anatolian Fault (Turkey) from Persistent Scatterer InSAR, *Geochem. Geophys. Geosyst.*, *15*, 2883–2894, doi:10.1002/2014GC005307.

Chaussard, E., R. Bürgmann, M. Shirzaei, E. J. Fielding, and B. Baker (2014), Predictability of hydraulic head changes and characterization of aquifer-system and fault properties from InSAR-derived ground deformation, *J. Geophys. Res. Solid Earth*, *119*, 6572–6590, doi:10.1002/2014JB011266.

Chaussard, E., R. Bürgmann, H. Fattahi, R. M. Nadeau, T. Taira, C. W. Johnson, and I. Johanson (2015), Potential for larger earthquakes in the East San Francisco Bay Area due to the direct connection between the Hayward and Calaveras Faults, *Geophys. Res. Lett.*, *42*, 2734–2741, doi:10.1002/2015GL063575.

Chen, C. W., and H. A. Zebker (2001), Two-dimensional phase unwrapping with use of statistical models for cost functions in nonlinear optimization, *J. Opt. Soc. Am. A*, *18*(2), 338–351.

Chen, K. H., R. M. Nadeau, and R.-J. Rau (2007), Towards a universal rule on the recurrence interval scaling of repeating earthquakes?, *Geophys. Res. Lett.*, *34* L16308, doi:10.1029/2007GL030554.

d'Alessio, M. A., I. A. Johanson, R. Bürgmann, D. A. Schmidt, and M. H. Murray (2005), Slicing up the San Francisco Bay Area: Block kinematics and fault slip rates from GPS-derived surface velocities, *J. Geophys. Res.*, *110*, B06403, doi:10.1029/2004JB003496.

Du, Y. J., and A. Aydin (1993), Stress transfer during 3 sequential moderate earthquakes along the central Calaveras Fault, California, *J. Geophys. Res.*, *98*(B6), 9947–9962.

Du, Y., A. Aydin, and P. Segall (1992), Comparison of various inversion techniques as applied to the determination of a geophysical deformation model for the 1983 Borah Peak earthquake, *Bull. Seismol. Soc. Am.*, *82*(4), 1840–1866.

Evans, E. L., J. P. Loveless, and B. J. Meade (2012), Geodetic constraints on San Francisco Bay Area fault slip rates and potential seismogenic asperities on the partially creeping Hayward Fault, *J. Geophys. Res.*, *117*, B03410, doi:10.1029/2011JB008398.

Farr, T. G., et al. (2007), The Shuttle Radar Topography Mission, *Rev. Geophys.*, *45*, RG2004, doi:10.1029/2005RG000183.

Fattahi, H., and F. Amelung (2013), DEM error correction in InSAR time series, *IEEE Trans. Geosci. Remote Sens.*, *51*(7), doi:10.1109/TGRS.2012.2227761.

Fattahi, H., and F. Amelung (2014), InSAR uncertainty due to orbital errors, *Geophys. J. Int.*, *199*(1), 549–560, doi:10.1093/gji/ggu276.

Ferretti, A., F. Novali, R. Bürgmann, G. Hilley, and C. Prati (2004), InSAR Permanent Scatterer analysis reveals ups and downs in San Francisco Bay area, *Eos Trans. AGU*, *85*(34), 317.

Fialko, Y. (2006), Interseismic strain accumulation and the earthquake potential on the southern San Andreas fault system, *Nature*, *441*(7096), 968–971, doi:10.1038/nature04797.

Field, E. H., et al. (2015), Long-term time-dependent probabilities for the Third Uniform California Earthquake Rupture Forecast (UCERF3), *Bull. Seismol. Soc. Am.*, doi:10.1785/0120140093.

Gilmore, T. D. (1993), Historical uplift measured across the eastern San Francisco Bay region, *Div. Mines Geol. Spec. Publ.*, *113*, 55–63.

Gourmelen, N., F. Amelung, and R. Lanari (2010), Interferometric synthetic aperture radar–GPS integration: Interseismic strain accumulation across the Hunter Mountain fault in the eastern California shear zone, *J. Geophys. Res.*, *115*, B09408, doi:10.1029/2009JB007064.

Graymer, R. W., D. A. Ponce, R. C. Jachens, R. W. Simpson, G. A. Phelps, and C. M. Wentworth (2005), Three-dimensional geologic map of the Hayward Fault, northern California: Correlation of rock units with variations in seismicity, creep rate, and fault dip, *Geology*, *33*(6), 521–524, doi:10.1130/G21435.1.

Hardebeck, J. L., and A. Aron (2009), Earthquake stress drops and inferred fault strength on the Hayward Fault, East San Francisco Bay, California, *Bull. Seismol. Soc. Am.*, *99*(3), 1801–1814, doi:10.1785/0120080242.

Hartzell, S. H., and T. H. Heaton (1986), Rupture history of the 1984 Morgan Hill, California, earthquake from the inversion of strong motion records, *Bull. Seismol. Soc. Am.*, *76*(3), 649–674.

Heidbach, O., M. Tingay, A. Barth, J. Reinecker, D. Kurfeß, and B. Müller (2008), The World Stress Map database release 2008, doi:10.1594/GFZ.WSM.Rel2008

Jachens, R. C., C. M. Wentworth, and R. W. Graymer (2002), A 40-km-long concealed basin suggests large offset on the Silver Creek fault, Santa Clara Valley, California *Geol Soc Am*, *Cordilleran Section - 98th Annual Meeting* (*May 13–15*, *2002*).

Jachens, R. C., G. A. Phelps, R. W. Simpson, R. W. Graymer, D. A. Ponce, and C. M. Wentworth (2003), Preliminary insights on Hayward Fault seismicity and geology: Results from analyzing a 3-dimensional geologic map of the Hayward Fault and vicinity, San Francisco Bay Region, California, in *Proceedings of the Hayward Fault Workshop, Eastern San Francisco Bay Area, California, September 19–20, 2003*, *U.S. Geol. Surv. Open File Rep*. 03–485, edited by D. A. Ponce et al., US Dep. of Interior and the US Geol. Surv., pp. 15–16.

Johnson, K. M., and J. Fukuda (2010), New methods for estimating the spatial distribution of locked asperities and stress-driven interseismic creep on faults with application to the San Francisco Bay Area, California, *J. Geophys. Res.*, *115*, B12408, doi:10.1029/2010JB007703.

Johnson, K. M., R. Bürgmann, and K. Larson (2006), Frictional properties on the San Andreas Fault near Parkfield, California, inferred from models of afterslip following the 2004 earthquake, *Bull. Seismol. Soc. Am.*, *96*(4B), S321–S338, doi:10.1785/0120050808.

Kelson, K. I., and G. D. Simpson (1995), *Late Quaternary Deformation of the Southern East Bay Hills*, vol. 79, pp. 590, American Association of Petroleum Geologists Bulletin, Alameda County, Calif.

Kelson, K. I., G. D. Simpson, C. C. Haraden, T. L. Sawyer, and M. A. Hemphill-Haley (1993), Late Quaternary surficial deformation of the Southern East Bay Hills, San Francisco Bay Region, California *final technical report for U.S. Geol. Surv. National Earthquake Hazard Reduction Program*, Award 1434-92-G-2209, 29 pp.

Ketelaar, G., F. Van Leijen, P. Marinkovic, and R. F. Hanssen (2007), *Multi-track PS-InSAR Datum Connection*, pp. 2481–2484 , IEEE, Barcelona.

Koltermann, C. E., and S. M. Gorelick (1992), Paleoclimatic signature in terrestrial flood deposits, *Science*, *256*(5065), 1775–1782, doi:10.1126/science.256.5065.1775.

Lanari, R., F. Casu, M. Manzo, and P. Lundgren (2007), Application of the SBAS-DInSAR technique to fault creep: A case study of the Hayward Fault, California, *Remote Sens. Environ.*, *109*(1), 20–28, doi:10.1016/j.rse.2006.12.003.

Lee, J. C., J. Angelier, H. T. Chu, J. C. Hu, F. S. Jeng, and R. J. Rau (2003), Active fault creep variations at Chihshang, Taiwan, revealed by creep meter monitoring, 1998–2001, *J. Geophys. Res.*, *108*(B11), 2528, doi:10.1029/2003JB002394.

Lienkaemper, J. J., and P. L. Williams (2007), A record of large earthquakes on the Southern Hayward Fault for the past 1800 years, *Bull. Seismol. Soc. Am.*, *97*(6), 1803–1819, doi:10.1785/0120060258.

Lienkaemper, J. J., G. Borchardt, and M. Lisowski (1991), Historic creep rate and potential for seismic slip along the Hayward Fault, California, *J. Geophys. Res.*, *96*(B11), 18,261–18,283.

Lienkaemper, J. J., F. S. McFarland, R. W. Simpson, R. G. Bilham, D. A. Ponce, J. J. Boatwright, and S. J. Caskey (2012), Long-term creep rates on the Hayward Fault: Evidence for controls on the size and frequency of large earthquakes, *Bull. Seismol. Soc. Am.*, *102*(1), 31–41, doi:10.1785/0120110033.

Lienkaemper, J. J., F. S. McFarland, R. W. Simpson, and S. J. Caskey (2014), Using surface creep rate to infer fraction locked for sections of the San Andreas fault system in Northern California from alignment array and GPS data, *Bull. Seismol. Soc. Am.*, *104*, 3094–3114, doi:10.1785/0120140117.

Lisowski, M., J. C. Savage, and W. H. Prescott (1991), The velocity field along the San Andreas Fault in central and southern California, *J. Geophys. Res.*, *96*(B5), 8369–8389.

Lockner, D. A., C. Morrow, D. Moore, and S. Hickman (2011), Low strength of deep San Andreas Fault gouge from SAFOD core, *Nature*, *472*(7341), 82–85, doi:10.1038/nature09927.

Lozos, J. C., D. D. Oglesby, J. N. Brune, and K. B. Olsen (2014), Rupture propagation and ground motion of strike-slip stepovers with intermediate fault segments, *Bull. Seismol. Soc. Am.*, *105*(1), 387–399, doi:10.1785/0120140114.

Malservisi, R., C. Gans, and K. P. Furlong (2003), Numerical modeling of strike-slip creeping faults and implications for the Hayward Fault, California, *Tectonophysics*, *361*(1–2), 121–137.

Manaker, D. M., R. Bürgmann, W. H. Prescott, and J. Langbein (2003), Distribution of interseismic slip rates and the potential for significant earthquakes on the Calaveras Fault, central California, *J. Geophys. Res.*, *108*(B6), 2287, doi:10.1029/2002JB001749.

Marinkovic, P., and Y. Larsen (2013), Consequences of long-term ASAR local oscillator frequency decay—An empirical study of 10 years of data, in *Proceedings of the Living Planet Symposium (abstract)*, European Space Agency, Edinburgh, U. K.

Marone, C. (1998), Laboratory-derived friction laws and their application to seismic faulting, *Annu. Rev. Earth Planet. Sci.*, *26*, 643–696, doi:10.2307/27878658?ref=no-x-route:6b049a5fe05c4b2a1b963e4198b20266.

Marone, C., and C. H. Scholz (1988), The depth of seismic faulting and the upper transition from stable to unstable slip regimes, *Geophys. Res. Lett.*, *15*(6), 621–624.

McLaughlin, R. J., W. V. Sliter, D. H. Sorg, P. C. Russell, and A. M. SarnaWojcicki (1996), Large-scale right-slip displacement on the East San Francisco Bay Region fault system, California: Implications for location of late Miocene to Pliocene Pacific Plate boundary, *Tectonics*, *15*(1), 1–18.

Meade, B. J. (2007), Algorithms for the calculation of exact displacements, strains, and stresses for triangular dislocation elements in a uniform elastic half space, *Comput. Geosci.*, *33*(8), 1064–1075, doi:10.1016/j.cageo.2006.12.003.

Moore, D. E., and D. A. Ponce (2001), Petrography and physical properties of selected rock types associated with the Hayward Fault, California U.S. Geol. Surv. Open File Rep., 01–263.

Murray, J., and J. Langbein (2006), Slip on the San Andreas Fault at Parkfield, California, over two earthquake cycles, and the implications for seismic hazard, *Bull. Seismol. Soc. Am.*, *96*(4), S283–S303, doi:10.1785/0120050820.

Murray, J., and P. Segall (2002), Testing time-predictable earthquake recurrence by direct measurement of strain accumulation and release, *Nature*, *419*(6904), 287–291, doi:10.1038/nature00984.

Murray-Moraleda, J. R., and R. W. Simpson (2009), Geodetically inferred coseismic and postseismic slip due to the *M* 5.4 31 October 2007 Alum Rock Earthquake, *Bull. Seismol. Soc. Am.*, *99*(5), 2784–2800, doi:10.1785/0120090017.

Nadeau, R. M. M., and L. R. Johnson (1998), Seismological studies at Parkfield VI: Moment release rates and estimates of source parameters for small repeating earthquakes, *Bull. Seismol. Soc. Am.*, *88*(3), 790–814.

NCEDC (2014), Northern California Earthquake Data Center. UC Berkeley Seismological Laboratory. Dataset. doi:10.7932/NCEDC.

Noda, H., and N. Lapusta (2013), Stable creeping fault segments can become destructive as a result of dynamic weakening, *Nature*, *493*(7433), 518–521, doi:10.1038/nature11703.

Oglesby, D. D. (2005), The dynamics of strike-slip step-overs with linking dip-slip faults, *Bull. Seismol. Soc. Am.*, *95*(5), 1604–1622, doi:10.1785/0120050058.
Okada, Y. (1985), Surface deformation due to shear and tensile faults in a half-space, *Bull. Seismol. Soc. Am.*, *75*, 1135–1154.
Oppenheimer, D. H., and A. G. Lindh (1992), The potential for earthquake rupture of the northern Calaveras Fault, in *Proceedings of the Second Conference on Earthquake Hazards in the Eastern San Francisco Bay Area*, *Spec. Publ. Calif. Div. Mines Geol.*, vol. 113, pp. 233–240, California Dep. of Conservation, Division of Mines and Geology, Sacramento.
Oppenheimer, D. H., P. A. Reasenberg, and R. W. Simpson (1988), Fault plane solutions for the 1984 Morgan Hill, California, earthquake sequence: Evidence for the state of stress on the Calaveras Fault, *J. Geophys. Res.*, *93*(B8), 9007–9026.
Oppenheimer, D. H., W. H. Bakun, and A. G. Lindh (1990), Slip partitioning of the Calaveras Fault, California, and prospects for future earthquakes, *J. Geophys. Res.*, *95*(B6), 8483–8498.
Oppenheimer, D. H., W. H. Bakun, T. Parsons, R. W. Simpson, J. Boatwright, and R. A. Uhrhammer (2010), The 2007 M5.4 Alum Rock, California, earthquake: Implications for future earthquakes on the central and southern Calaveras Fault, *J. Geophys. Res.*, *115*, B08305, doi:10.1029/2009JB006683.
Peng, Z., J. E. Vidale, C. Marone, and A. Rubin (2005), Systematic variations in recurrence interval and moment of repeating aftershocks, *Geophys. Res. Lett.*, *32*, L15301, doi:10.1029/2005GL022626.
Pepe, A., and R. Lanari (2006), On the extension of the minimum cost flow algorithm for phase unwrapping of multitemporal differential SAR interferograms, *IEEE Trans. Geosci. Remote Sens.*, *44*(9), 2374–2383, doi:10.1109/TGRS.2006.873207.
Ponce, D. A., T. G. Hildenbrand, R. C. Jachens, C. W. Roberts, and P. E. Fahringer (1998), Gravity and magnetic anomalies along the Hayward Fault and their relation to earthquake seismicity, California (abstract) *Eos Trans. AGU*, *79*(45), Fall Meet. Suppl., F594.
Ponce, D. A., T. G. Hildenbrand, and R. C. Jachens (2003), Gravity and magnetic expression of the San Leandro gabbro with implications for the geometry and evolution of the Hayward fault zone, northern California, *Bull. Seismol. Soc. Am.*, *93*, 14–26.
Ponce, D. A., R. W. Graymer, R. C. Jachens, R. A. Williams, R. W. Simpson, C. M. Wentworth, and C. W. Roberts (2005), Southern extension of the Hayward Fault and its relationship to the Calaveras and Silver Creek Faults northern California, GSA Abs. with Prog., Ann. Cordilleran Sect. Mtg., San Jose, April 29–May 1, p. 90.
Prescott, W. H., and M. Lisowski (1983), Strain accumulation along the San-Andreas fault system east of San-Francisco Bay, California, *Tectonophysics*, *97*(1–4), 41–56.
Resor, P. G. (2003), Deformation associated with continental normal faults, PhD dissertation, Stanford Univ.
Rivera, L., and H. Kanamori (2002), Spatial heterogeneity of tectonic stress and friction in the crust, *Geophys. Res. Lett.*, *29*(6), 1088, doi:10.1029/2001GL013803.
Rosen, P. A., S. Hensley, G. Peltzer, and M. Simons (2004), Update repeat orbit interferometry package released, *Eos Trans. AGU*, *85*, 47.
Savage, J. C., and R. O. Burford (1973), Geodetic determination of relative plate motion in Central California, *J. Geophys. Res.*, *78*(5), 832–845.
Schleicher, A. M., B. A. van der Pluijm, and L. N. Warr (2010), Nanocoatings of clay and creep of the San Andreas Fault at Parkfield, California, *Geology*, *38*(7), 667–670, doi:10.1130/G31091.1.
Schmidt, D. A., R. Bürgmann, R. M. M. Nadeau, and M. d'Alessio (2005), Distribution of aseismic slip rate on the Hayward Fault inferred from seismic and geodetic data, *J. Geophys. Res.*, *110*, B08406, doi:10.1029/2004JB003397.
Schwartz, D. P., P. J. Haeussler, G. G. Seitz, and T. E. Dawson (2012), Why the 2002 Denali fault rupture propagated onto the Totschunda fault: Implications for fault branching and seismic hazards, *J. Geophys. Res.*, *117*, B11304, doi:10.1029/2011JB008918.
Shimazaki, K., and T. Nakata (1980), Time-predictable recurrence model for large earthquakes, *Geophys. Res. Lett.*, *7*(4), 279–282.
Shirzaei, M. (2015), A seamless multitrack multitemporal InSAR algorithm, *Geochem. Geophys. Geosyst.*, *16*, 1656–1669, doi:10.1002/2015GC005759.
Shirzaei, M., and R. Bürgmann (2013), Time-dependent model of creep on the Hayward Fault from joint inversion of 18 years of InSAR and surface creep data, *J. Geophys. Res. Solid Earth*, *118*, 1733–1746, doi:10.1002/jgrb.50149.
Sieh, K., and P. L. Williams (1990), Behavior of the Southernmost San-Andreas Fault during the past 300 years, *J. Geophys. Res.*, *95*(B5), 6629–6645.
Simpson, G. D., J. N. Baldwin, K. I. Kelson, and W. R. Lettis (1999), Late Holocene slip rate and earthquake history for the northern Calaveras Fault at Welch Creek, eastern San Francisco Bay area, California, *Bull. Seismol. Soc. Am.*, *89*(5), 1250–1263.
Simpson, R. W., J. J. Lienkaemper, and J. S. Galehouse (2001), Variations in creep rate along the Hayward Fault, California, interpreted as changes in depth of creep, *Geophys. Res. Lett.*, *28*(11), 2269–2272.
Templeton, D. C., R. M. Nadeau, and R. Burgmann (2009), Distribution of postseismic slip on the Calaveras Fault, California, following the 1984 *M*6. 2 Morgan Hill earthquake, *Earth Planet. Sci. Lett.*, *277*(1), 1–8, doi:10.1016/j.epsl.2008.09.024.
Tizzani, P., P. Berardino, F. Casu, P. Euillades, M. Manzo, G. P. Ricciardi, G. Zeni, and R. Lanari (2007), Surface deformation of Long Valley Caldera and Mono Basin, California, investigated with the SBAS-InSAR approach, *Remote Sens. Environ.*, *108*(3), 277–289, doi:10.1016/j.rse.2006.11.015.
Tong, X., D. T. Sandwell, and B. R. Smith-Konter (2013), High-resolution interseismic velocity data along the San Andreas Fault from GPS and InSAR, *J. Geophys. Res. Solid Earth*, *118*, 369–389, doi:10.1029/2012JB009442.
Toppozada, T. R., and G. Borchardt (1998), Re-evaluation of the 1836 "Hayward Fault" and the 1838 San Andreas Fault earthquakes, *Bull. Seismol. Soc. Am.*, *88*, 140–159.
Toppozada, T. R., D. M. Branum, M. S. Reichle, and C. L. Hallstrom (2002), San Andreas fault zone, California: $M \geq 5.5$ earthquake history, *Bull. Seismol. Soc. Am.*, *92*, 2555–2601.
Wakabayashi, J. (1999), Distribution of displacement on and evolution of a young transform fault system: The northern San Andreas fault system, California, *Tectonics*, *18*(6), 1245–1274.
Waldhauser, F., and W. L. Ellsworth (2000), A double-difference earthquake location algorithm: Method and application to the northern Hayward Fault, California, *Bull. Seismol. Soc. Am.*, *90*(6), 1353–1368.
Waldhauser, F., and W. L. Ellsworth (2002), Fault structure and mechanics of the Hayward Fault, California, from double-difference earthquake locations, *J. Geophys. Res.*, *107*(B3), 2054, doi:10.1029/2000JB000084.
Waldhauser, F., and D. P. Schaff (2008), Large-scale relocation of two decades of Northern California seismicity using cross-correlation and double-difference methods, *J. Geophys. Res.*, *113*, B08311, doi:10.1029/2007JB005479.
Watt, J. T., R. W. Graymer, R. W. Simpson, D. A. Ponce, R. C. Jachens, G. A. Phelps, and C. M. Wentworth (2007), A Three-dimensional geologic model of the Hayward-Calaveras Fault junction Eos Trans. AGU, vol. 88, no. 52, Fall Meet. Suppl.
Williams, R. A., W. J. Stephenson, C. M. Wentworth, K. J. Odum, R. T. Hanson, and R. C. Jachens (2002), Definition of the Silver Creek Fault and Evergreen Basin sediments from seismic reflection data San Jose, California, *AGU Fall Meeting*.
Wilson, A. M., and S. Gorelick (1996), The effects of pulsed pumping on land subsidence in the Santa Clara Valley, California, *J. Hydrol.*, *174*(3), 375–396.
Wright, T. J., B. E. Parsons, and Z. Lu (2004), Toward mapping surface deformation in three dimensions using InSAR, *Geophys. Res. Lett.*, *31* L01607, doi:10.1029/2003GL018827.

Yu, E., and P. Segall (1996), Slip in the 1868 Hayward earthquake from the analysis of historical triangulation data, *J. Geophys. Res.*, *101*(B7), 16,101–16,118.

Zhang, H. J., and C. H. Thurber (2003), Double-difference tomography: The method and its application to the Hayward Fault, California, *Bull. Seismol. Soc. Am.*, *93*(5), 1875–1889.

Zhao, P., and Z. Peng (2008), Velocity contrast along the Calaveras Fault from analysis of fault zone head waves generated by repeating earthquakes, *Geophys. Res. Lett.*, *35*, L01303, doi:10.1029/2007GL031810.

Journal of Geophysical Research

Supporting Information for

Interseismic deformation and refined earthquake potential on the Hayward-Calaveras Fault system

E. Chaussard [1,2,3], R. Bürgmann [1,2], H. Fattahi [4], C.W. Johnson [1,2], R. Nadeau [1,2], T. Taira[1,2], and I. Johanson [1,2]

(1) Department of Earth and Planetary Science, University of California, Berkeley, Berkeley, California

(2) Berkeley Seismological Laboratory, University of California, Berkeley, California

now at (3) Department of Geology, State University of New York, Buffalo, New York

(4) Seismological Laboratory, California Institute of Technology, Pasadena, California

Contents of this file

Path	Frame	Orbit	ERS	Env	Time
70	2853	Desc	75	31	1992-2011
299	2853	Desc	75	23	1992-2011
206	747	Asc	0	25	2003-2010
206	729	Asc	0	27	2003-2010
478	747	Asc	29	22	1995-2011
478	729	Asc	19	13	2001-2011

Table S1. Number of ERS and Envisat SAR acquisitions processed for each track and frame of the InSAR time series analysis.

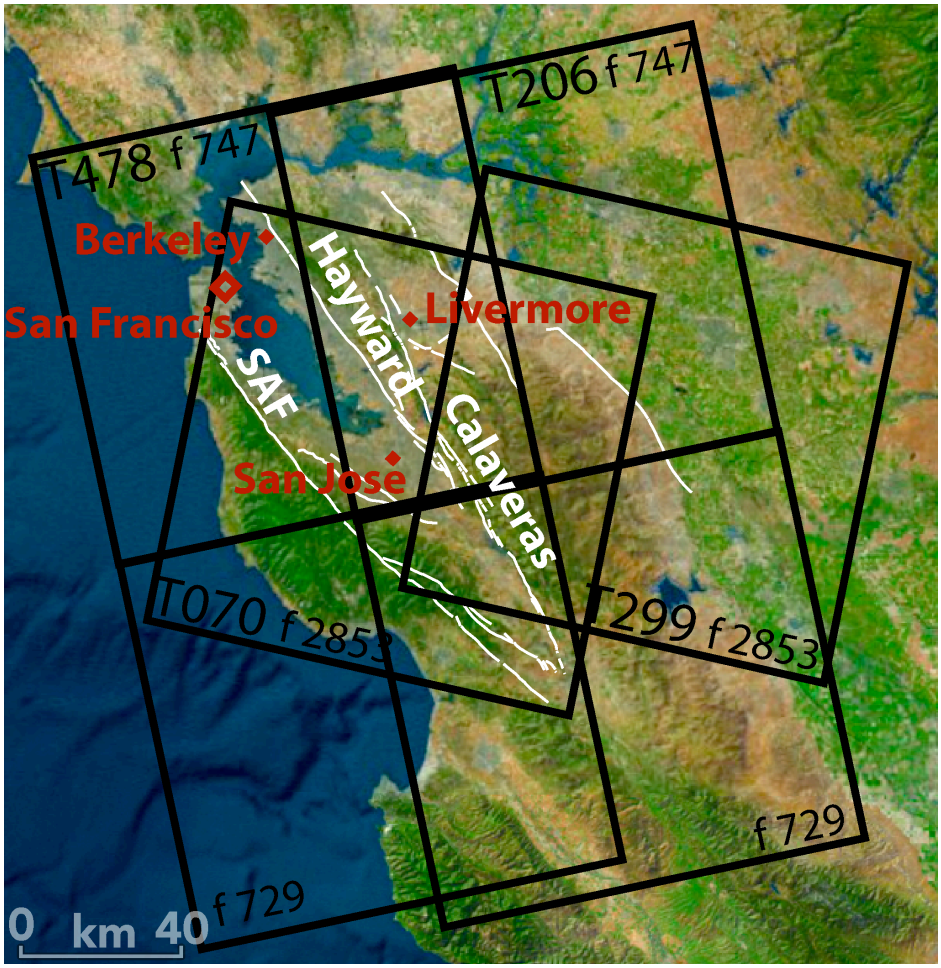

Figure S1. Track and frame locations (black rectangles) of the SAR data processed for the 1992-2011 InSAR time series analysis (Table 1). The white lines indicate the main faults and the red diamonds the main cities.

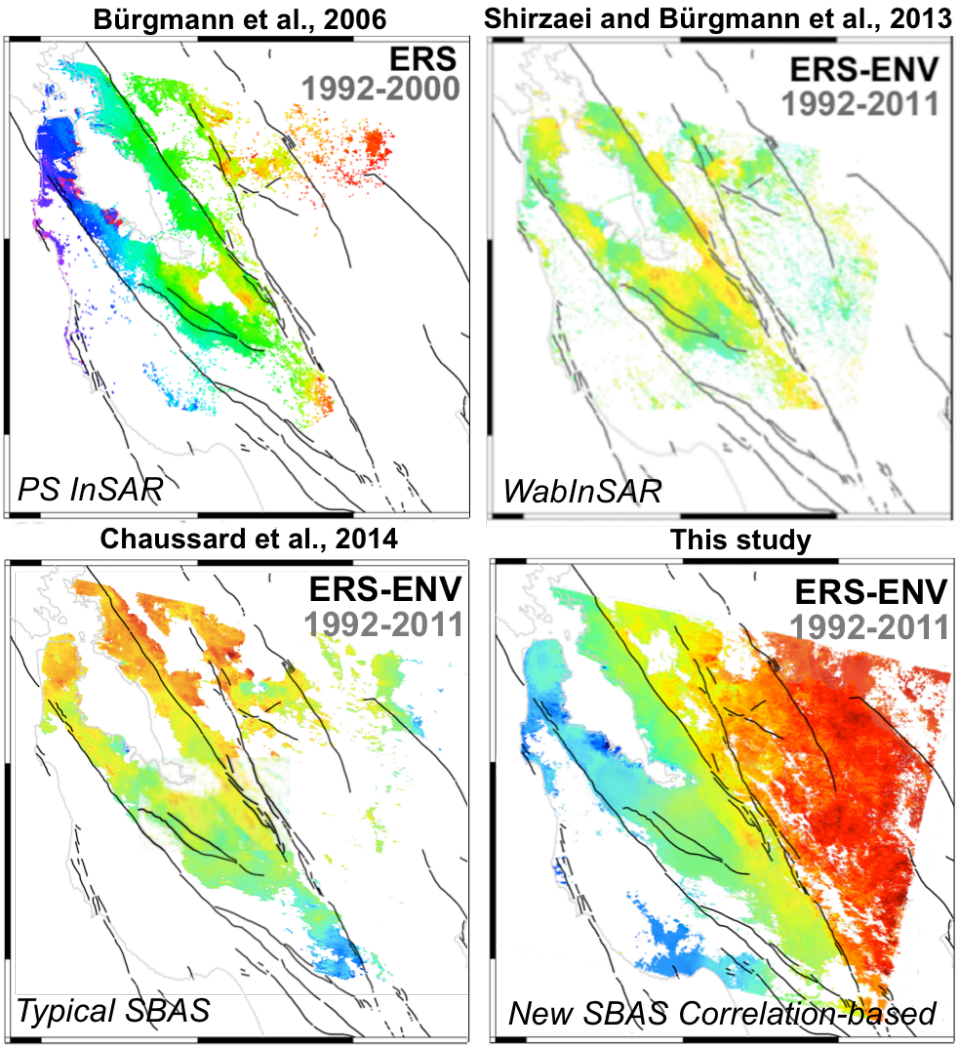

Figure S2. Mean LOS InSAR velocity maps from previous works illustrating the current weaknesses of typical InSAR processing for interseismic deformation: long-wavelength deformation from strain accumulation is missed (ramp removal in processing) and loss of coherence in vegetated areas (East San Francisco Bay), compared to our results (bottom right).

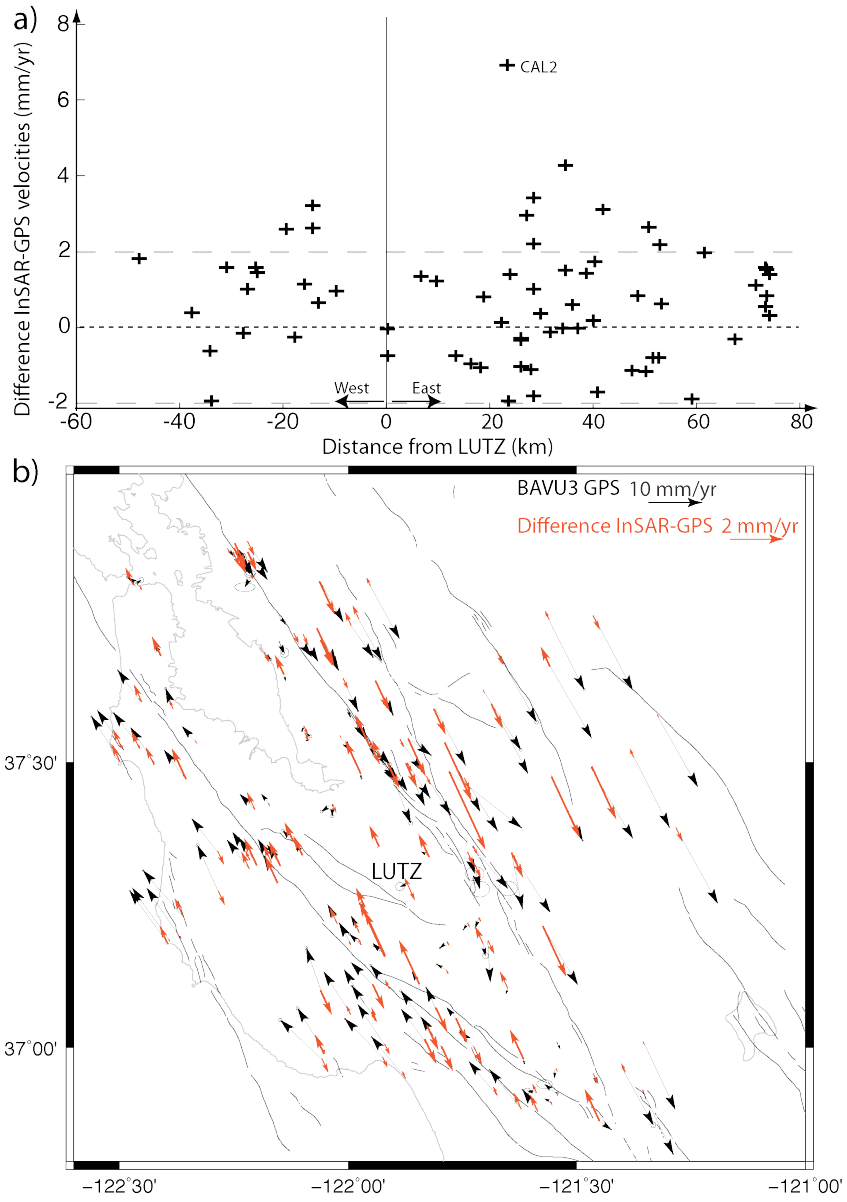

Figure S3. a) Difference (misfit) between the horizontal InSAR and horizontal GPS velocities shown as a function of the distance from the reference station LUTZ. b) Same in map view for the misfit in the fault parallel-direction (red arrows) compared to the BAVU3 velocities (black arrows) with different scales. The lack of a clear relationship between InSAR-GPS difference and the distance from the reference suggests that the source of the misfit is due to errors in the GPS data and turbulent tropospheric noise in the InSAR rather that remaining orbital errors.

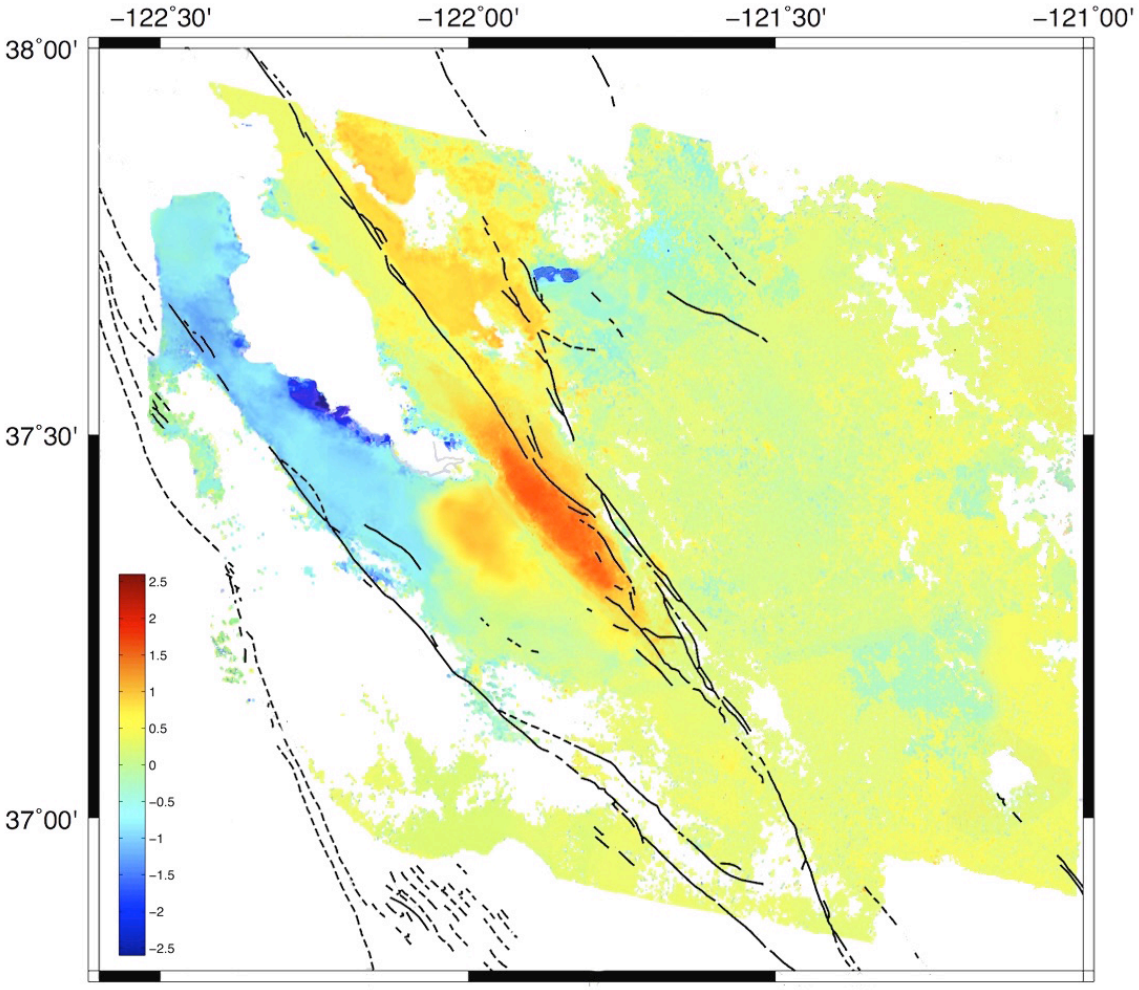

Figure S4. Mean vertical ground velocity map with a saturated color-scale (±2.5 mm/yr). Full and dashed black lines indicate mapped fault traces.

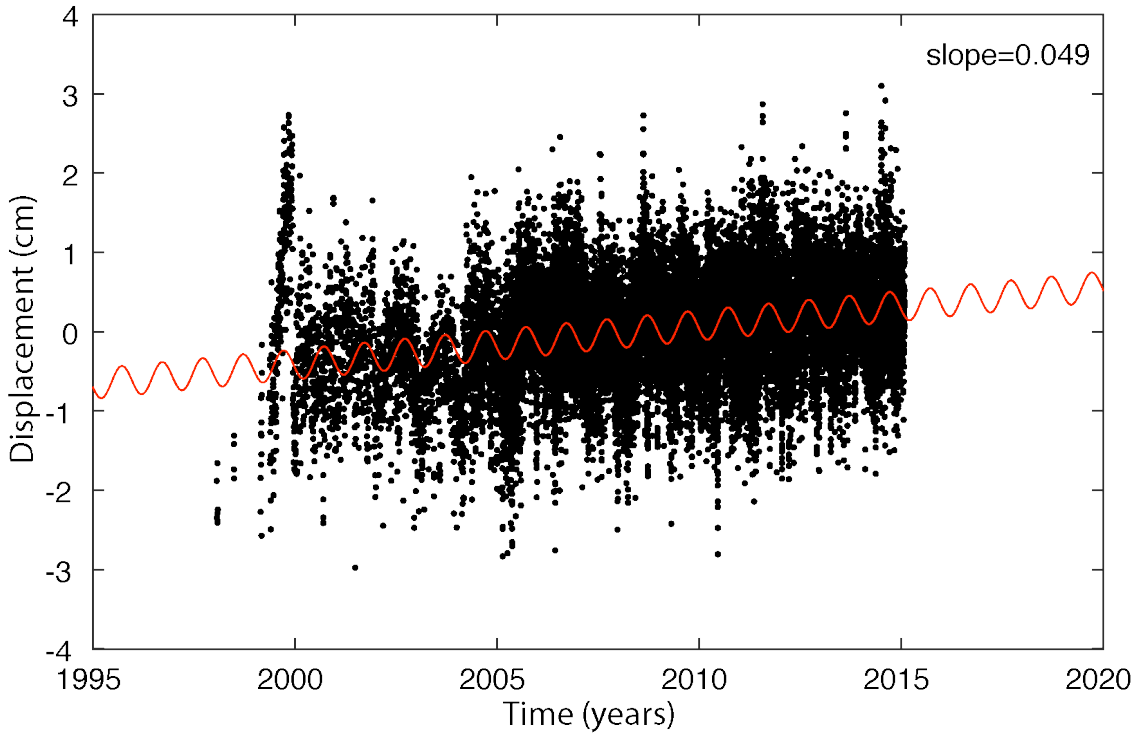

Figure S5. Difference between time series of continuous GPS sites in the East Bay Hills and sites to the west (near the Bay, not in coastal areas) and to the east (near Mount Diablo). The slope suggest uplift of the East Bay Hills at 0.5 mm/yr agreeing with the lower bound estimate of the mean InSAR vertical velocity map. However, the large amount of noise and scatter in these time series suggest that longer observations are necessary to extract a reliable signal.

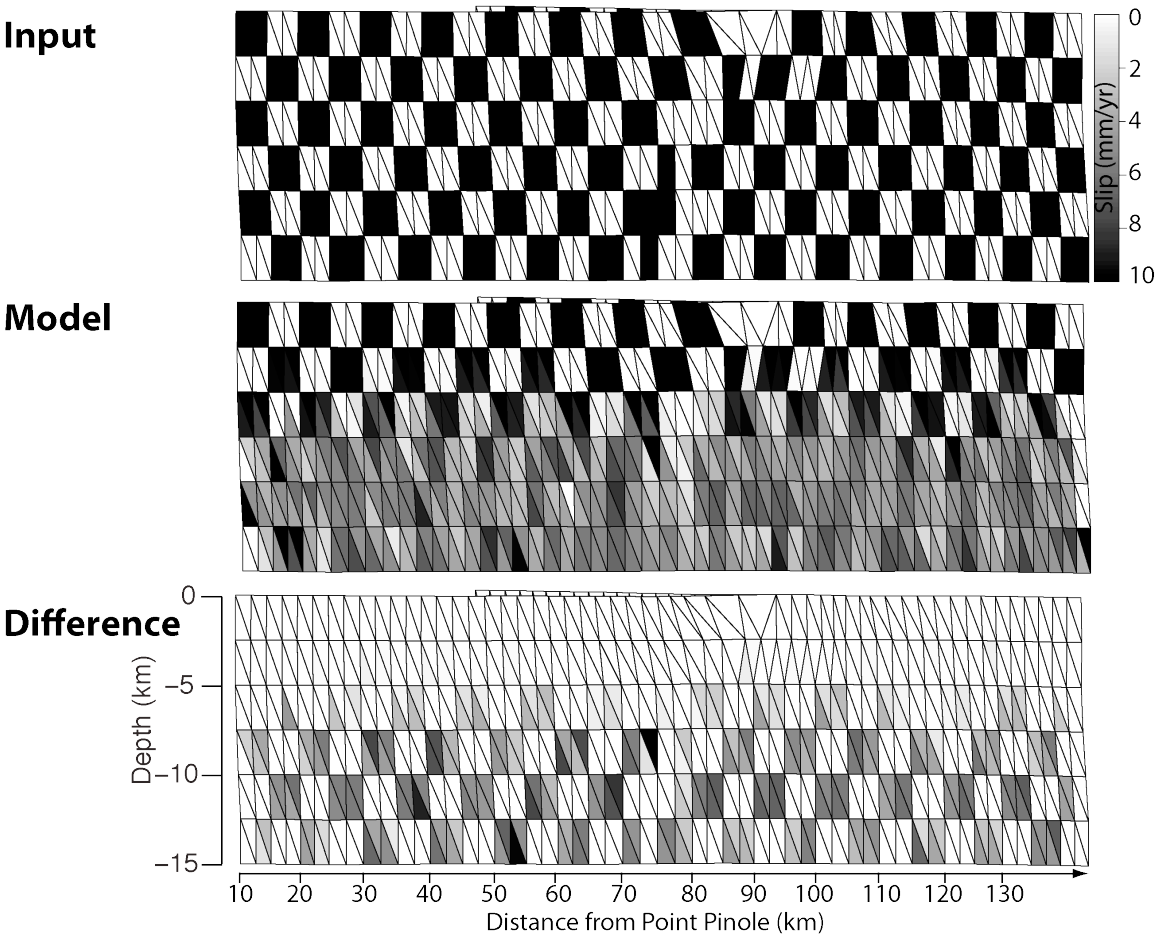

Figure S6. Checkerboard test for the shallow slip model. The top panel shows the input slip for a forward model to create a simulated velocity field, the middle panel shows the recovered slip from inversion of the simulated velocity field, and the bottom panel the difference between the two. The model resolution is significantly decreasing for depths greater than 7.5 km.

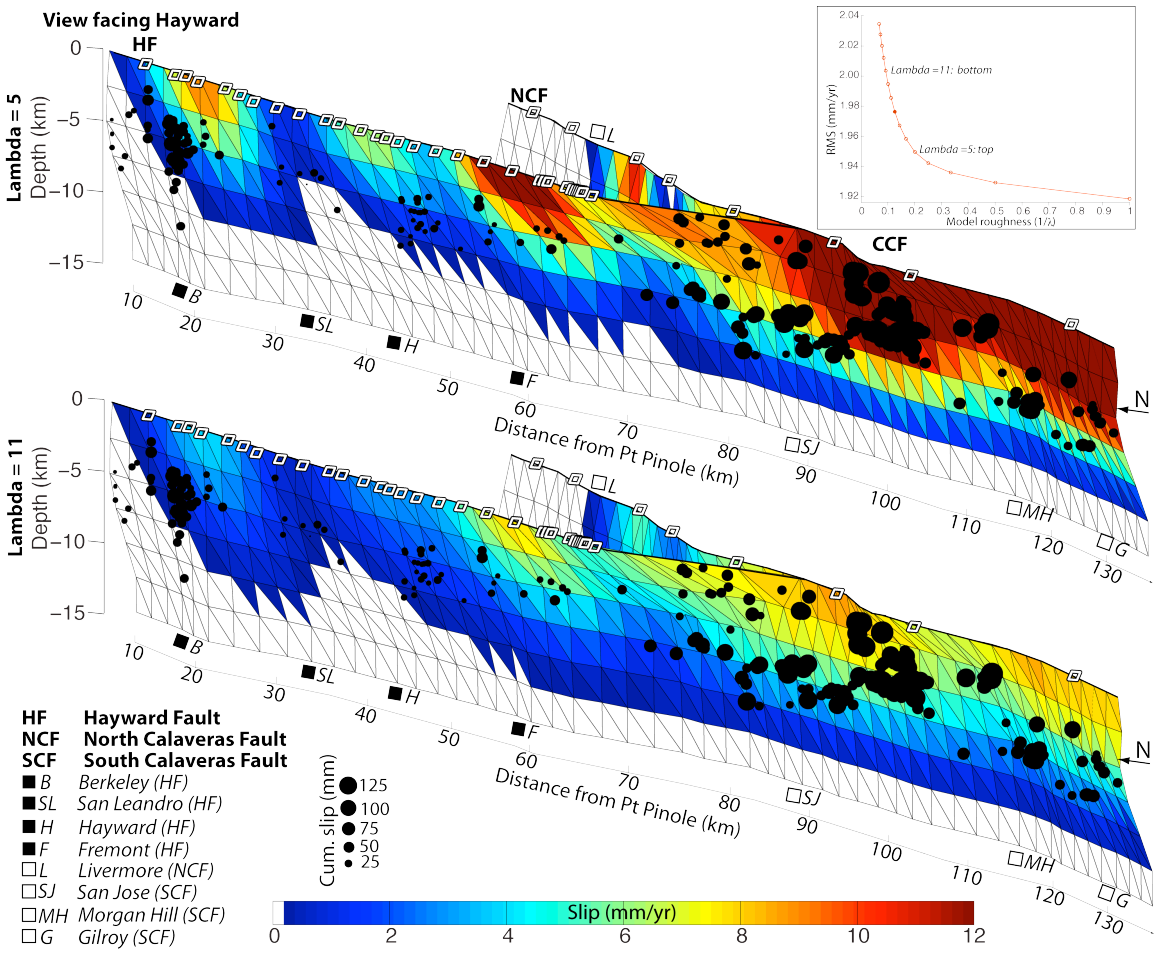

Figure S7. Example of models of slip distribution from surface creep using low (top, λ=5) and high (bottom, λ=11) smoothing factors.

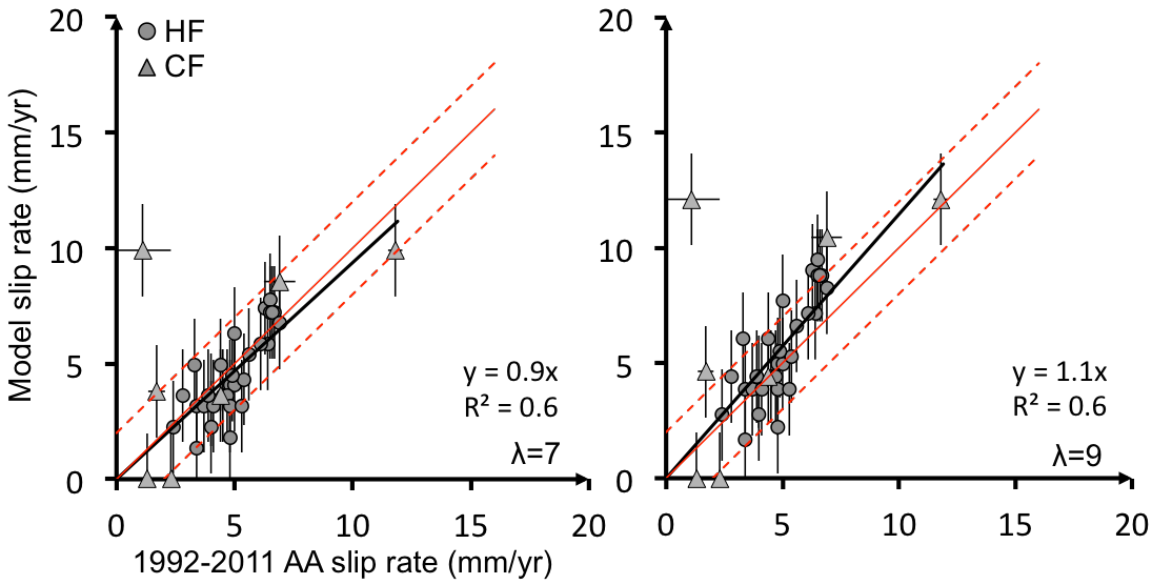

Figure S8. Comparison between slip rates produced by models with lower (left) and higher (right) Laplacian smoothing operators (λ) than the best fitting model (λ=8) at the locations of the HF AAs (dots) and the CF AAs (triangles) compared to the surface creep between 1992-2011 measured by AAs. The full red line shows a 1-to-1 linear regression and the two dashed red lines ±2 mm/yr deviation (confidence level of the InSAR data). The black line shows the best fitting linear regression with the parameters shown in the bottom right. The model with the best fitting Laplacian smoothing operator show a linear regression with a slope of 1 between the modeled and observed surface slip rates while the models with lower and higher Laplacian smoothing operators have lower and higher slopes, respectively.